This is the peer-reviewed, final accepted version for American Mineralogist, published by the Mineralogical Society of America.
The published version is subject to change. Cite as Authors (Year) Title. American Mineralogist, in press.
DOI: https://doi.org/10.2138/am-2022-8615. http://www.minsocam.org/

Revision 1

Identifying xenocrystic tourmaline in Himalayan leucogranites

Jinsheng Han[1], Huayong Chen[2, *], Haijun Xu[3, *], Olivier Nadeau[4], Chang Xu[3]

[1]*State Key Laboratory of Geological Processes and Mineral Resources, and School of Earth Resources, China University of Geosciences, Wuhan (CUGW) 430074, China*

[2]*Key Laboratory of Mineralogy and Metallogeny, Guangzhou Institute of Geochemistry, Chinese Academy of Sciences, Guangzhou 510640, China*

[3]*State Key Laboratory of Geological Processes and Mineral Resources, and School of Earth Sciences, CUGW*

[4]*Laboratory for Isotopes in Economic Geology and its Environment (LIEGE), Department of Mineral Resources and Engineering, School of Earth Sciences, CUGW*

*Correspondence to huayongchen@gig.ac.cn and hj_xu@sina.com

ABSTRACT

Tourmaline is a common autocrystic mineral in granitic and pegmatitic rocks that records valuable information on the physicochemical evolution of magmas. However, xenocrystic tourmaline that does not crystallize from host magmas are also common but seldom reported, and notoriously difficult to identify. Here, autocrystic (Tur G) and xenocrystic (Tur P) tourmalines are identified in two-mica granites and granitic pegmatites from the Cuonadong leucogranites, eastern Himalaya. Electron backscatter diffraction (EBSD), coupled with electron-probe micro-analysis (EPMA) and laser ablation ICP-MS analyses (LA-ICP-MS), is used to discriminate xenocrystic from autocrystic tourmaline. Although both tourmalines have slightly different chemical compositions, the differences are not sufficient for their unambiguous

discrimination. However, EBSD systematically shows complex intra-crystalline orientations and deformation for xenocrystic grains, and undeformed crystal lattices are predominant in autocrystic grains. EBSD could be a useful tool to identify the origin of tourmaline in granitic rock, particularly useful when geochemical analyses and/or geochronological measurements are impractical.

KEY WORDS:

Autocrystic and xenocrystic tourmaline, boron isotopes, Cuonadong leucogranites, electron backscattered diffraction analyses, Himalayan granites

INTRODUCTION

Tourmaline occurs in granitic rocks and related pegmatites and mineral deposits (van Hinsberg et al., 2011a, b) and is stable over wide ranges of pressures (P) and temperatures (T) (Dutrow and Henry, 2011). It accommodates a diversity of elements and has extremely low rates of intracrystalline diffusion (van Hinsberg et al., 2011a, b). This makes tourmaline a valuable archive of the physicochemical conditions under which it grew (Marschall and Jiang, 2011; Slack and Trumbull, 2011). As a result, tourmaline has been widely used to study magmatic-hydrothermal evolution (e.g. Yang et al., 2015; Launay et al., 2018), ore-forming processes (e.g. Slack and Trumbull, 2011; Su et al., 2019), fluid-rock interactions (e.g. Trumbull et al., 2009; Berryman et al., 2017), and subduction-zone fluid compositions (van Hinsberg et al., 2017). These studies combined macro-textural observations with geochemical data to distinguish between tourmaline populations. In this study, compositional and isotopic information from the techniques EPMA, LA-ICP-MS and multiple collector LA-ICP-MS (LA-MC-ICP-MS) analyses is insufficient to discriminate between tourmaline populations that are suspected to have different origins. However, micro-textural and crystallographic data from EBSD studies discriminates

between two populations, one of which is proposed to be xenocrystic, and the other, autocrystic.

SAMPLE CONTEXT

The collision between India and Asia occurred at ca. 60 Ma and the subsequent breakoff of the subducted Neo-Tethyan slab occurred at ca. 45 Ma. However, intra-continental processes that followed collision occurred at the Miocene (Wu et al., 2019; Han et al., 2020). The Cuonadong leucogranites are located in the easternmost section of the Tethyan Himalaya, and are related to the Indian plate rollback and breakoff during the intra-continental processes (DeCelles et al., 2011), and are associated with Be-Sn-W mineralization (Cao et al., 2021). The leucogranites consist mainly of two-mica granites, muscovite granites and granitic pegmatites, and were produced by multistage anatexis during the Tertiary (45–16 Ma; Cao et al., 2021; Fan et al., 2021). The two-mica granites and granitic pegmatites (Fig. 1A) are the main hosts of tourmaline, lack apparent deformation, and yielded comparable monazite U-Th-Pb crystallization ages of 20.3 ± 0.2 and 20.5 ± 0.1 Ma (Han et al., 2020), respectively. The comparable ages, together with their similar mineral assemblages consisting of plagioclase, k-feldspar, muscovite ± tourmaline and the occurrence of pegmatite veins in the two-mica granite, without clear boundaries between them, as well as Zr/Hf in zircons, suggest that the Miocene two-mica granite evolved to the Miocene granitic pegmatite by fractional crystallization (Han et al., 2020; Xie et al., 2020). However, two xenocrystic monazite grains yielding older ages of 45.2 ± 1.6 and 43.9 ± 1.4 Ma were also identified in the two-mica granites (Han et al., 2020). Tourmaline crystals from the two-mica granite (Tur G; Fig. 1B) are small (1–3 mm), coexist with quartz, muscovite, plagioclase, and K-feldspar, and occur as disseminated inter-granular euhedral needles and were considered as autocrystic crystals crystallized from the Miocene two-mica granite. They also commonly show core-rim zoning and are thus subdivided into Tur G-cores and Tur G-rims. By

contrast, tourmaline crystals from the pegmatites (Tur P; Fig. 1C) are large (3–8 cm) and are systematically separated by quartz ± feldspar-bearing fractures (Fig. 1C). Quartz ± feldspar-bearing fractures traversing tourmaline crystals may also be coeval with the evolution of the host granitoids and such tourmaline crystals may also be autocrystic ones. Any dissolution or overgrowth texture was not found on the Tur P. However, the Tur P previously yielded an $^{40}Ar/^{39}Ar$ mini-plateau age of ca. 43 Ma, similar to that of the xenocrystic monazite, also indicating a xenocrystic origin, 20 My. earlier than the Miocene pegmatite (Han et al., 2020). Some other minerals such as quartz and/or feldspar may also be xenocrystic.

ANALYTICAL METHODS

The major element compositions of tourmalines were determined at the State Key Laboratory of Geological Process and Mineral Resources, China University of Geoscience, Wuhan, China (GPMR) using a JEOL JXA-8230 Electron Probe Micro Analyzer (EPMA) with an accelerating voltage of 15 kV, a beam current of 10 nA, and a beam diameter of 5 μm. The counting time for peaks and backgrounds were 10 s and 5 s, respectively, for all elements. The following standards were used: hornblende for Si, Mg and Ca, rutile for Ti, cordierite for Al, fayalite for Fe, rhodonite for Mn, jadeite for Na, sanidine for K and topaz for F. Data were corrected on-line using a ZAF (atomic number, adsorption, fluorescence) correction procedure. Tourmaline structural formulae were calculated by normalizing to 15 cations per formula unit (pfu) in the tetrahedral and octahedral sites (T + Z + Y) (Henry and Dutrow, 1996), based on the general formula $XY_3Z_6T_6O_{18}(BO_3)_3V_3W$, where X = Na, Ca, K, vacancies; Y = Fe, Mg, Mn, Ti, Al; Z = Al, Mg; T = Si, Al; B = B; V = OH^- and O^{2-}; W = OH^-, F^- and O^{2-}. During the calculation, we assume 3 B pfu, ignoring any tetrahedral B and assume there is no O at V site and calculating Fe^{2+} vs Fe^{3+} by charge balance. Such calculation yields the minimum amount of Fe^{3+} in the

tourmaline. The maximum estimate of Fe^{3+} is calculated by treating all Fe as ferric and calculating the ratio of O/OH at the VW sites. In such calculation, V + W = OH + O + F = 4 (Berryman et al., 2017). The method yielding the minimum amount of Fe^{3+} in the tourmaline is more realistic because it results in the presence of both Fe^{2+} and Fe^{3+} in the normalized tourmaline formula.

Trace element compositions were obtained on the same spots at the In situ Mineral Geochemistry Lab, Ore Deposit and Exploration Centre (ODEC), Hefei University of Technology, China, using an Agilent 7900 Quadrupole ICP-MS coupled to a Photon Machines Analyte HE 193 nm ArF Excimer laser ablation system. The ablation protocol was performed using a laser diameter of 44 μm with a repetition rate of 8 Hz and an energy of ~4 J/cm^2. Measurements were conducted during 40 s after 20 s of gas blank. Standard reference materials BCR-2G and NIST SRM 610 and 612 glasses were analyzed after every eight spot analysis. The raw data was processed using the procedure of Berryman et al. (2017), and using the Iolite data processing software. The concentration of major elements (Na, Ca, K, Mg, Fe, Si) was also measured and used to normalize the data to 15 cations at the Y, Z, and T sites, as was done with the EMPA data. Such method of normalization avoids relying on a nonideal internal standard.

Boron isotopic compositions were measured on the same spots or nearby area at the Beijing Createch Testing Technology Co., Ltd, Beijing, China, using a Neptune Plus MC-ICP-MS and ESI NWR213 laser-ablation system. The ablation protocol was performed with a diameter of 60 μm at 10 Hz with energy of ~4 J/cm^2 for 40 s after measuring the gas blank for 20 s. Carrier gas consisting of mixed He, Ar, and N was used to carry the aerosols to the plasma. The ratios of $^{11}B/^{10}B$ in tourmalines and standards were collected statically and simultaneously using two Faraday cups. The standard sample-standard bracketing (SSB) method and the tourmaline

115 standard IAEA B4 ($\delta^{11}B$ = -8.71‰, Tonarini et al., 2003) were adopted as external standards to
116 calibrate the instrument. Through repeated analysis of tourmaline reference material IMR RB1
117 ($\delta^{11}B$ = -12.96 ± 0.97‰, Hou et al., 2010), the SSB method was used to evaluate the analytical
118 quality and instrument mass fractionation (IMF). Instrumental mass fractionation (IMF) and
119 analytical quality were assessed by replicate analysis of tourmaline reference materials schorl
120 (HS #112566) from the Harvard Mineralogical Museum (Dyar et al., 2000). The similarity of
121 IMF values (Table S3) determined for the tourmaline standards demonstrates a lack of significant
122 chemical matrix effect with our analytical setup. The analytical precision was estimated to be
123 better than 0.5‰ based on replicate analyses of monitored tourmalines.

124 The crystallographic orientation of tourmaline was determined using an Oxford Instruments
125 HKL Nordlys II EBSD detector and AZtecHKL 5.0 software coupled to a ZEISS Sigma 300 VP
126 Field Emission scanning electron microscope (SEM), housed in the School of Earth Sciences,
127 China University of Geoscience, Wuhan, China. Working conditions were as follows: 20 kV
128 accelerating voltage, working distance of ~18 mm and 70° sample tilt under low vacuum
129 conditions (20 Pa of N gas) to avoid excessive electron charging. Orientation maps were
130 acquired in automatic mode with a step size of 41 μm for Tur-P and 5 μm for Tur-G. To assure
131 data quality, only those measurements with mean angular deviation values below 1.0º (between
132 detected and 199 simulated EBSD patterns) were accepted for analyses. The EBSD data clean up
133 and post-processing were analyzed using Oxford Instruments HKL Channel5 software. More
134 details can be found in Liu et al. (2021).

135 **RESULTS**

136 **Tourmaline Compositions**

Both the Tur G (including cores and rims) and Tur P tourmalines belong to the alkali group of the X-site occupancy classification diagram (Henry et al., 2011a, b) (Fig. 2A), and plot in the field of Li-poor granitoids and associated pegmatites and aplites in the diagrams using the molar Al-Fe-Mg subsystem of Henry and Guidotti (1985) and Henry and Dutrow (2018) (Figs. 2B and 2C). All tourmalines plot in the schorl (Fe-rich) field (Fig. 2D), with Mg/(Mg+Fe) and Na/(Na+Ca) ratios ranging from 0.19–0.24 and 0.93–0.98, respectively, for the Tur G-cores, 0.10–0.16 and 0.93–0.98, respectively, for the Tur G-rims and 0.19–0.30 and 0.82–0.96, respectively, for the Tur P (Table S1). Relative to Tur G, the Tur P has higher Mg, Ti, and Mg#, as well as more vacancies in the X-site (Table S1). The Fe vs. Mg diagram indicates the important influence of $(X_{\square}Al)(NaMg)_{-1}$ substitution for the Tur P whereas the Tur G was influenced by the $Fe^{2+}Mg_{-1}$ and $(X_{\square}Al)(NaMg)_{-1}$ substitution (Fig. 2E). Meanwhile, the Al_{tot} vs. $X_{\square}$ diagram indicates the influence of $(X_{\square}Al_2)(CaMg_2)_{-1}$ substitution (Fig. 2F).

Most trace elements in tourmalines have median concentrations ranging from 0.1 to tens of ppm, in addition to slightly higher concentrations of Cr and Li (Fig. 3; Table S2). The Tur G has lower concentrations of Be, Sc, V, Co, Cr, Ni, Sr, Ta and higher concentrations of Li, Sn than the Tur P (Fig. 3). All tourmalines have very low REE concentrations, and enriched chondrite-normalized light REE (LREE) compared to heavy REE (HREE) (Table S2).

The Tur G tourmalines have higher $\delta^{11}B$ values than the Tur P tourmalines (Fig. 4A). The $\delta^{11}B$ values range from -8.1 to -7.3 ‰ (average -7.3 ‰, n=26) in Tur G, and from -10.6 to -9.2 ‰ (average -10.1 ‰, n=47; Table S4) in Tur P. Both families of tourmaline plot within the fields of worldwide granites/pegmatites, continental crust, and mantle and mid-ocean ridge basalts (MORB), although a part of the Tur P plot outside the field of mantle and MORB (Fig. 4B).

These ranges in $\delta^{11}B$ values are relatively narrow and overlap significantly, so the present differences in $\delta^{11}B$ values are inconclusive in terms of B sources.

Crystallographic Features of Tourmalines

Coexisting grains of Tur G show no clear relations in crystallographic orientations on the orientation map using inverse pole figure color scheme (Fig. 5A) and the pole figure for crystallographic orientations (Fig. 5B). The texture component map of grain #G1 shows very limited intracrystalline misorientation of 0–3° with respect to the reference orientation (yellow cross; Fig. 5C). The total cumulative misorientation across the #G1 grain is ≤2° along the orthogonal a-a' and b-b' cross-sections (Fig. 5D).

Although the Tur P tourmaline also coexists with quartz and minor feldspars, it is shattered into fragments of irregular shapes having grain sizes ranging from <1 mm to 1 cm (Fig. 1C). Numerous tourmaline grains are strongly variegated in color and contain abundant intracrystalline low angle (2° and 5°) boundaries in the crystallographic orientation EBSD map (Fig. 6A). Several relationships exist in the crystallographic orientations amongst independent tourmaline grains. For example, the #P1 and #P2 grains are parallel to the $\{10\bar{1}0\}$ plane, and the #P3 and #P4 grains have very similar orientations, as shown in the equal area upper hemisphere projection orientation (UHPO) pole map (Fig. 6B). The Tur P grains additionally display intragranular misorientation of up to 10° with respect to the reference orientation (yellow cross; Fig. 6C). The misorientation profiles along cross-sections x-x' (#P1) and y-y' (#P3) (Fig. 6D) show maximum cumulative misorientations reaching up to ~12°, with misorientations between adjacent points reaching as much as ~8°.

DISCUSSION AND IMPLICATIONS

Comparison of Tur G and Tur P Tourmalines

Before discussing the tourmaline geochemistry, it is important to restate two facts: 1) the Miocene two-mica granite evolved to the Miocene granitic pegmatite by fractional crystallization; 2) the Tur G are autocrystic crystals crystallized from the Miocene two-mica granite whereas the Tur P yielding an $^{40}Ar/^{39}Ar$ mini-plateau age of ca. 43 Ma contained in the Miocene pegmatite as xenocrystic crystals (Han et al., 2020). Given the small tourmaline-melt partition coefficients for most elements at high temperatures, tourmaline may efficiently be used to document the evolution of the magmas (Balen and Broska, 2011; Drivenes et al., 2015; Roda-Robles et al., 2015). The Tur G coexist with quartz, muscovite, plagioclase, and K-feldspar, and occur as disseminated inter-granular euhedral needles, indicating that they are autocrystic crystals in the two-mica granite (Figs. 1B and 5A). However, the origin of the Tur P remains to be uncertain as they were xenocrysts in the pegmatite and no more information were known except for that they were separated by quartz ± feldspar-bearing fractures. Here, both the Tur G and the Tur P tourmalines plot within the field of Li-poor granitoids and associated pegmatites and aplites using the molar Al-Fe-Mg subsystem of Henry and Guidotti (1985) and Henry and Dutrow (2018) (Figs. 2B and 2C). This suggests that both families of tourmaline likely formed in magmatic environments. The tourmalines in our study have compositions that are similar to the magmatic tourmalines of the Gurla Mandhata tourmaline leucogranite, Northwest Himalaya and the Nyalam leucogranite, South Tibetan Himalaya (Figs. 2A and 2B; Yang et al., 2015; Cheng et al., 2021), further suggesting the magmatic origin of the Cuonadong tourmalines.

The $\delta^{11}B$ values of the Tur P and the Tur G both lie in the field of worldwide granites and pegmatites (Fig. 4B). In combination with comparable monazite U-Th-Pb ages of ~20 Ma (Han et al., 2020), a previous study of Zr/Hf in zircons concluded that the two-mica granite evolved to the granitic pegmatite by fractional crystallization (Xie et al., 2020). Given that such fractional

crystallization is commonly accompanied by fluid exsolution and melt devolatilization (second boiling), and since ^{11}B is preferentially partitioned in the fluid phase over the melt during devolatilization (Jiang et al., 1998; Hervig et al., 2002; Maner and London, 2018), the lighter $\delta^{11}B$ values in the pegmatite-hosted Tur P (avg. -10.1 ‰) than the two-mica granite-hosted Tur G (avg. -7.3 ‰) (Fig. 4A) could *a priori* be explained by fractional crystallization and gradual devolatilization, which is contrary to the fact that the Tur G are autocrystic crystals crystallized from the Miocene two-mica granite whereas the Tur P as xenocrystic crystals crystallized from an Eocene pegmatite.

In a closed system, major elements in tourmalines are usually controlled by intensive thermodynamic parameters such as P and T whereas trace element abundances are normally governed by partitionning amongst the different phases in presence (e.g., Van Hingsberg, 2011a, b; Klemme et al., 2011). However, in certain circumstances, the major and trace element concentrations in tourmaline were both controlled by intensive thermodynamic parameters coupled with substitution mechanisms, as correlations occurred between trace and major elements such as Fe/(Fe+Mg) or Ca/(Ca+Na) (Marks et al., 2013; Harlaux et al., 2020; Zhao et al., 2021). Here, the Tur G are relatively enriched in Li and Sn, whereas the Tur P have higher contents of Be, Sc, V, Co, Cr, Ni, Sr and Ta (Fig. 3), but no statistically valid correlations are identified between Fe/(Fe+Mg) and Ca/(Ca+Na) on the one hand, and most trace elements on the other hand (Figs. 7, 8). The absence of statically valid correlations between trace and major elements preclude the influence of intensive thermodynamic parameters coupled with substitution mechanisms on the trace elements concentrations in tourmalines. The higher concentrations of Li and Sn in the Tur G and the higher contents of Be, Sc, V, Co, Cr, Ni, Sr and Ta in the Tur P are thus taken to reflect the compositional differences of the melt from which

they grew, which is in agreement with the assertion that tourmaline chemistry mostly reflect the compositional nature of its host melt (van Hinsberg, 2011a, b). As the Miocene two-mica granite evolved to the Miocene granitic pegmatite by fractional crystallization, the autocrystic tourmalines in the Miocene granitic pegmatite should have higher Li and lower Sc, V, Cr, Ni, Sr contents than Tur G in the Miocene two-mica granite. Then the lower Li and higher Sc, V, Cr, Ni, Sr contents of Tur P further support that they were not autocrystic tourmalines in the Miocene granitic pegmatite.

Discrimination of Autocrystic and Xenocrystic Tourmalines

Although age discrepancies between host magmatic rocks and xenocrystic mineral grains may directly discriminate autocrystic and xenocrystic mineral grains, many minerals are notoriously difficult, and possibly impossible to date, and the age difference obtained for minerals that are possible to date may fall within the range of analytical uncertainty. Furthermore, differences in compositions between different generations of individual minerals are usually inconclusive in terms of age, and may be ambiguous. Although the compositions of the Tur P and Tur G grains are somewhat similar, the crystallographic features of the tourmalines established using EBSD allow discriminating the xenocrystic Tur P from the autocrystic Tur G tourmaline grains.

In undeformed granitoids that are not affected by any mechanical disturbations, any autocrystic crystals crystallized from the melt will have very weak intracrystalline deformation and should be randomly distributed, without any obvious mineral orientation. Although the #G1, #G2 and #G3 tourmaline crystals from the two-mica granite occur together in the crytallographic orientation map (Fig. 5A), they appear disseminated throughout the sample in the UHPO pole map (Fig. 5B). Very few low-angle boundaries are observed in these grains (Fig. 5A), and other

tourmaline crystals from this sample share similar microstructural characteristics. These euhedral tourmaline crystals with randomly distributed orientations and deficient of low-angle boundaries have very weak intracrystalline deformation (Figs. 5C and 3D) and are typical of autocrystic crystals in undeformed granitoids.

By contrast, in the pegmatite, the #P1, #P2, #P3, and #P4 grains clearly display a restricted amount of distinct orientations (Figs. 6A and 4B). According to the UHPO pole map, the #P3 and #P4 grains have a very similar orientation (Fig. 6B), whereas the #P1 and #P2 grains are parallel to one (1010) plane (Fig. 6B). Abundant, discrete low-angle boundaries are observed in the Tur P (Figs. 6A and 6C), which also display cumulative intragranular misorientations reaching up to 10° across the grain, and misorientations between adjacent points as large as ~8° (Figs. 6C and 6D). This is taken to indicate that the xenocrystic "Tur P" were affected by deformation. Combined with textural petrographic information, the relations of orientation between these tourmaline grains indicate that they were likely xenocrysts as a single tourmaline crystal which was subsequently torn apart into multiple fragments during deformation. The EBSD data thus provide quantitative evidence of crystal-plastic and brittle deformation of the Tur P. As the comagmatic Miocene (ca. 20 Ma) two-mica granites and pegmatites were not influenced by later deformation (Fig. 1A), which is here supported by the lack of deformation of the Tur G, the deformation of Tur P highlighted here must have occurred during or before the Miocene magmatism, thus evidencing their xenocrystic origin.

Implications

Isotope geochronology and mineral chemistry may in some cases be incapable of discriminating xenocrystic from autocrystic crystals. Electron backscatter diffraction (EBSD) analyses focusing on intracrystalline deformation and crystallographic relations may nevertheless

prove useful and provide critical information discriminating grains of different generations. The EBSD method is applied here for the first time on tourmaline and can be used in conjunction with- and in support of *in situ* geochronology, and may also be used to discriminate xenocrystic from autocrystic grains when geochronology data is not available, or when the age differences are smaller than the related analytical uncertainties.

ACKNOWLEDGMENTS

This study was funded by the National Natural Science Foundation of China (41725009, 42173068), the Fundamental Research Funds for the Central Universities (CUG2106201), China University of Geosciences (Wuhan), and the Fundamental and Applied Fundamental Research Major Program of Guangdong Province (2019B030302013).

REFERENCES CITED

Balen, D., and Broska, I. (2011) Tourmaline nodules: Products of devolatilization within the final evolutionary stage of granitic melt? Geological Society, London, Special Publications, 350, 53–68.

Berryman, E.J., Kutzschbach, M., Trumbull, R.B., Meixner, A., van Hinsberg, V., Kasemann, S.A., and Franz, G. (2017) Tourmaline as a petrogenetic indicator in the Pfitsch Formation, Western Tauern Window, Eastern Alps. Lithos, 284-285 (Special issue), 138–155.

Cao, H.W., Li, G.M., Zhang, R.Q., Zhang, Y.H., Zhang, L.K., Dai, Z.W., Zhang, Z., Liang, W., Dong, S.L., and Xia, X.B. (2021) Genesis of the Cuonadong tin polymetallic deposit in the Tethyan Himalaya: Evidence from geology, geochronology, fluid inclusions and multiple isotopes. Gondwana Research, 92, 72–101.

Cheng, L., Zhang, C., Liu, X., Yang, X., Zhou, Y., Horn, I., Weyer, S., and Holtz, F. (2021) Significant boron isotopic fractionation in the magmatic evolution of Himalayan leucogranite recorded in multiple generations of tourmaline. Chemical Geology, 571, 120194, DOI: 10.1016/j.chemgeo.2021.120194.

Codeço, M.S., Weis, P., Trumbull, R.B., Pinto, F., Lecumberri-Sanchez, P., and Wilke, F.D. (2017) Chemical and boron isotopic composition of hydrothermal tourmaline from the Panasqueira W-Sn-Cu deposit, Portugal. Chemical Geology, 468, 1–16.

Dyar, M.D., Wiedenbeck, M., Robertson, D., Cross, L.R., Delaney, J.S., Ferguson, K., Francis, C.A., Grew, E.S., Guidotti, C.V., Hervig, R.L., Hughes, J.M., Husler, J., Leeman, W., McGuire, A.V., Rhede, D., Rothe, H., Paul, R.L., Richards, I., and Yates, M. (2001) Reference minerals for the microanalysis of light elements. Geostandards Newsletter, 25, 441–463.

DeCelles, P.G., Kapp, P., Quade, J., and Gehrels, G.E. (2011) Oligocene–Miocene Kailas basin, southwestern Tibet: Record of postcollisional upper-plate extension in the Indus-Yarlung suture zone. Geological Society of America Bulletin, 123 (7-8), 1337–1362.

Drivenes, K., Larsen, R.B., Müller, A., Sørensen, B.E., Wiedenbeck, M., and Raanes, M.P. (2015) Late-magmatic immiscibility during batholith formation: assessment of B isotopes and trace elements in tourmaline from the Land's End granite, SW England. Contributions to Mineralogy and Petrology, 169, 1–27.

Dutrow, B.L., and Henry, D.J. (2011) Tourmaline: A Geologic DVD. Elements, 7, 301–306.

Fan, J.J., Wang, Q., Li, J., Wei, G.J., Ma, J.L., Ma, L., Li, Q.W., Jiang, Z.Q., Zhang, L., Wang, Z.L., and Zhang, L. (2021) Boron and molybdenum isotopic fractionation during crustal anatexis: Constraints from the Conadong leucogranites in the Himalayan Block, South Tibet. Geochimica et Cosmochimica Acta, 297, 120–142.

Han, J.S., Hollings, P., Jourdan, F., Zeng, Y.C., and Chen, H.Y. (2020) Xenocrystic Eocene magmatic tourmaline captured by the Miocene Himalayan leucogranites. American Mineralogist, 105, 1436–1440.

Harlaux, M., Kouzmanov, K., Gialli, S., Laurent, O., Rielli, A., Dini, A., Chauvet, A., Menzies, A., Kalinaj, M., and Fontboté, L. (2020) Tourmaline as a Tracer of Late-Magmatic to Hydrothermal Fluid Evolution: The World-Class San Rafael Tin (-Copper) Deposit, Peru. Economic Geology, 115, 1665–1697.

Henry, D.J., and Guidotti, C.V. (1985) Tourmaline as a petrogenetic indicator mineral-An example from the staurolite-grade metapelites of NW Maine. American Mineralogist, 70, 1–15.

Henry, D.J., and Dutrow, B.L. (1996) Metamorphic tourmaline and its petrologic applications. Reviews in Mineralogy and Geochemistry, 33, 503–557.

Henry, D.J., Novak, M., Hawthorne, F.C., Ertl, A., Dutrow, B.L., Uher, P., and Pezzotta, F. (2011) Nomenclature of the tourmaline-supergroup minerals. American Mineralogist, 96, 895–913.

Henry, D.J., and Dutrow, B.L. (2018) Tourmaline studies through time: Contributions to scientific advancements. Journal of Geosciences (Czech Republic), 63, 77–98.

Hervig, R.L., Moore, G.M., Williams, L.B., Peacock, S.M., Holloway, J.R., and Roggensack, K. (2002) Isotopic and elemental partitioning of boron between hydrous fluid and silicate melt. American Mineralogist, 87, 769–774.

Hou, K.J., Li, Y.H., Xiao, Y.K., Liu, F., and Tian, Y.R. (2010) In situ boron isotope measurements of natural geological materials by LA-MC-ICP-MS. Chinese Science Bulletin, 55, 3305–3311.

Jiang, S.Y., and Palmer (1998) Boron isotope systematics of tourmaline from granites and pegmatites: A synthesis. European Journal of Mineralogy, 10, 1253–1265.

Klemme, S., Marschall, H.R., Jacob, D.E., Prowatke, S., and Ludwig, T. (2011) Trace-element partitioning and boron isotope fractionation between white mica and tourmaline. The Canadian Mineralogist, 49, 165–176.

Liu, W.L., Xu, H.J., and Shi, F. (2021) Decorated dislocations in naturally deformed olivine with C-type fabric: A case study in the Lüliangshan garnet peridotite from the North Qaidam ultrahigh-pressure belt, NW China. Tectonophysics, 814, 228971, DOI: 10.1016/j.tecto.2021.228971.

Launay, G., Sizaret, S., Guillou-Frottier, L., Gloaguen, E., and Pinto, F. (2018) Deciphering fluid flow at the magmatic-hydrothermal transition: A case study from the world-class

353 Panasqueira W–Sn–(Cu) ore deposit (Portugal). Earth and Planetary Science Letters, 499,
354 1–12.
355 Maner, J.L., and London, D. (2018) Fractionation of the isotopes of boron between granitic melt
356 and aqueous solution at 700 °C and 800 °C (200 MPa). Chemical Geology, 489, 16–27.
357 Marks, M.A., Marschall, H.R., Schühle, P., Guth, A., Wenzel, T., Jacob, D.E., Barth, M., and
358 Markl, G. (2013) Trace element systematics of tourmaline in pegmatitic and hydrothermal
359 systems from the Variscan Schwarzwald (Germany): The importance of major element
360 composition, sector zoning, and fluid or melt composition. Chemical Geology, 344, 73–90.
361 Marschall, H.R., and Jiang, S.Y. (2011) Tourmaline Isotopes: No Element Left Behind.
362 Elements, 7, 313–319.
363 Pal, D.C., Trumbull, R.B., and Wiedenbeck, M. (2010) Chemical and boron isotope
364 compositions of tourmaline from the Jaduguda U (–Cu–Fe) deposit, Singhbhum shear zone,
365 India: Implications for the sources and evolution of mineralizing fluids. Chemical Geology,
366 277, 245–260.
367 Roda-Robles, E., Simmons, W., Pesquera, A., Gil-Crespo, P.P., Nizamoff, J., and Torres-Ruiz, J.
368 (2015) Tourmaline as a petrogenetic monitor of the origin and evolution of the Berry-Havey
369 pegmatite (Maine, U.S.A.). American Mineralogist, 100, 95–109.
370 Slack, J.F., and Trumbull, R.B. (2011) Tourmaline as a Recorder of Ore-Forming Processes.
371 Elements, 7, 321–326.
372 Su, Z.K., Zhao, X.F., Zeng, L.P., Zhao, K.D., and Hofstra, A.H. (2019) Tourmaline boron and
373 strontium isotope systematics reveal magmatic fluid pulses and external fluid influx in a
374 giant iron oxide-apatite (IOA) deposit. Geochimica et Cosmochimica Acta, 259, 233–252.
375 Tonarini, S., Forte, C., Petrini, R., and Ferrara, G. (2003) Melt/biotite $^{11}B/^{10}B$ isotopic
376 fractionation and the boron local environment in the structure of volcanic glasses.
377 Geochimica et Cosmochimica Acta, 67, 1863–1873.
378 Trumbull, R.B., Krienitz, M.-S., Grundmann, G., and Wiedenbeck, M. (2009) Tourmaline
379 geochemistry and δ11B variations as a guide to fluid–rock interaction in the Habachtal
380 emerald deposit, Tauern Window, Austria. Contributions to Mineralogy and Petrology, 157,
381 411–427.
382 van Hinsberg, V. J., Franz, G., and Wood, B.J. (2017) Determining subduction-zone fluid
383 composition using a tourmaline mineral probe. Geochemical Perspectives Letters, 160–169.
384 van Hinsberg, V. J., Henry, D.J., and Dutrow, B.L. (2011a) Tourmaline as a Petrologic Forensic
385 Mineral: A Unique Recorder of Its Geologic Past. Elements, 7, 327–332.
386 van Hinsberg, V. J., Henry, D.J., and Marschall, H.R. (2011b) Tourmaline: an ideal indicator of
387 its host environment. The Canadian Mineralogist, 49, 1–16.
388 Wu, F.-Y., Liu, X.-C., Liu, Z.-C., Wang, R.-C., Xie, L., Wang, J.-M., Ji, W.-Q., Yang, L., Liu,
389 C., Khanal, G.P., and He, S.-X., 2020, Highly fractionated Himalayan leucogranites and
390 associated rare-metal mineralization: Lithos, 352-353, p. 105319, doi:
391 10.1016/j.lithos.2019.105319.
392 Xie, L., Tao, X., Wang, R., Wu, F., Liu, C., Liu, X., Li, X., and Zhang, R. (2020) Highly
393 fractionated leucogranites in the eastern Himalayan Cuonadong dome and related magmatic
394 Be–Nb–Ta and hydrothermal Be–W–Sn mineralization. Lithos, 354-355, 105286, DOI:
395 10.1016/j.lithos.2019.105286.
396 Yang, S.Y., Jiang, S.Y., and Palmer, M.R. (2015) Chemical and boron isotopic compositions of
397 tourmaline from the Nyalam leucogranites, South Tibetan Himalaya: Implication for their
398 formation from B-rich melt to hydrothermal fluids. Chemical Geology, 419, 102–113.

Zhao, H.D., Zhao, K.D., Palmer, M.R., Jiang, S.Y., and Chen, W. (2021) Magmatic-Hydrothermal Mineralization Processes at the Yidong Tin Deposit, South China: Insights from In Situ Chemical and Boron Isotope Changes of Tourmaline. Economic Geology, 116, 1625–1647.

FIGURE CAPTIONS

Figure 1. Photographs and photomicrographs showing field relations and typical mineral paragenesis and microstructures of the Cuonadong leucogranites, eastern Himalaya. (A) Field occurrence of tourmaline from the Cuonadong two-mica granite and pegmatite; (B) cross-polarized light photomicrograph showing the mineralogy and textural relations in the two-mica granite. Note the autocrystic tourmaline (Tur G) circled in red; (C) plane-polarized light photomicrograph highlighting the coarse-grained and fragmented texture of xenocrystic tourmaline (Tur P) from the pegmatite.

Figure 2. (A) Tourmaline X-site occupancy classification diagram (Henry et al., 2011) showing alkali-group tourmalines from the Cuonadong leucogranites; (B) upper half of the ternary Al-Fe-Mg diagram showing the fields of: (1) Li-rich granitoids and associated pegmatites and aplites; (2) Li-poor granitoids and associated pegmatites and aplites; (3) Fe^{3+}-rich quartz–tourmaline-bearing hydrothermally altered granites; (4) metapelites and metapsammites coexisting with an Al-saturated phase; (5) metapelites and metapsammites not coexisting with an Al-saturated phase; (6) Fe^{3+}-rich quartz–tourmaline-bearing rocks, calc silicate rocks, and metapelites; (7) low-Ca meta-ultramafics and Cr-V-rich metasediments; and (8) marbles and metapyroxenites (Henry and Guidotti, 1985). All autocrystic Tur G and xenocrystic Tur P tourmalines from the Cuonadong leucogranites plot in the field of Li-poor granitoids and associated pegmatites and aplites; (C) Diagram correlating tourmaline compositions with source-rock type using the molar

Al-Fe-Mg subsystem (Henry and Dutrow, 2018); (D) Atomic Mg/(Mg+Fe) vs. Na/(Na+Ca) diagram showing the fields of schorl and dravite; (E) Mg vs. Fe diagram expressed in atoms per formula unit (a.p.f.u.) showing the fields of schorl, dravite, foitite and Mg-foitite. Both the Mg/(Mg+Fe) vs. Na/(Na+Ca) and the Mg vs. Fe diagrams are from Pal et al. (2010); (F) Plot of Al vs. X-site vacancy.

Figure 3. Box-whisker plots showing the trace element composition of tourmalines from the Cuonadong leucogranites, eastern Himalaya, China.

Figure 4. (A) Boron isotopic composition of the Tur P and Tur G tourmalines from the Cuonadong leucogranites, eastern Himalaya; (B) comparison of the B isotopic composition of different B reservoirs (Marschall and Jiang, 2011).

Figure 5. Electron backscattered diffraction (EBSD) analyses of autocrystic Tur G tourmaline from the Cuonadong two-mica granite. (A) Orientation map using inverse pole figure color scheme (IPF-X, where X is vertical on the map). Low-angle boundaries are color-coded as a function of misorientations according to the legend in the panel; (B) pole figure for the orientation of {0001}, $\{10\bar{1}0\}$ and $\{11\bar{2}0\}$ crystallographic orientations in the upper hemisphere equal area projections of the orientations (UHPO); (C) texture component map of the #G1 tourmaline grain, color-coded for misorientation angles from the yellow "+"; (D) misorientation profiles of #G1 tourmaline grain along the a-a' and b-b' cross-sections shown in (C).

446 **Figure 6.** EBSD analysis of xenocrystic Tur P tourmaline from the Cuonadong pegmatite. (A)
447 Orientation map using inverse pole figure color scheme (IPF-X, where X is vertical on the map).
448 Low-angle boundaries are color-coded as a function of misorientations according to the legend in
449 the panel; (B) pole figure for the orientation of {0001}, $\{10\bar{1}0\}$ and $\{11\bar{2}0\}$ crystallographic in
450 the upper hemisphere equal area projections of the orientations (UHPO); (C) texture component
451 maps of #P1 and #P3 tourmaline grains from (A), color-coded for disorientation angle from the
452 yellow "+"; (D) misorientation profiles along the x-x' (in #P1) and y-y' (in #P3) cross-sections
453 shown in (C).
454
455 **Figure 7.** Binary plots showing the concentration of selected trace elements as a function of
456 Mg/(Mg+Fe) in tourmalines from the Cuonadong leucogranites.
457
458 **Figure 8.** Binary plots showing the concentration of selected trace elements as a function of
459 Ca/(Ca+Na) in tourmalines from the Cuonadong leucogranites.
460

Figure 1

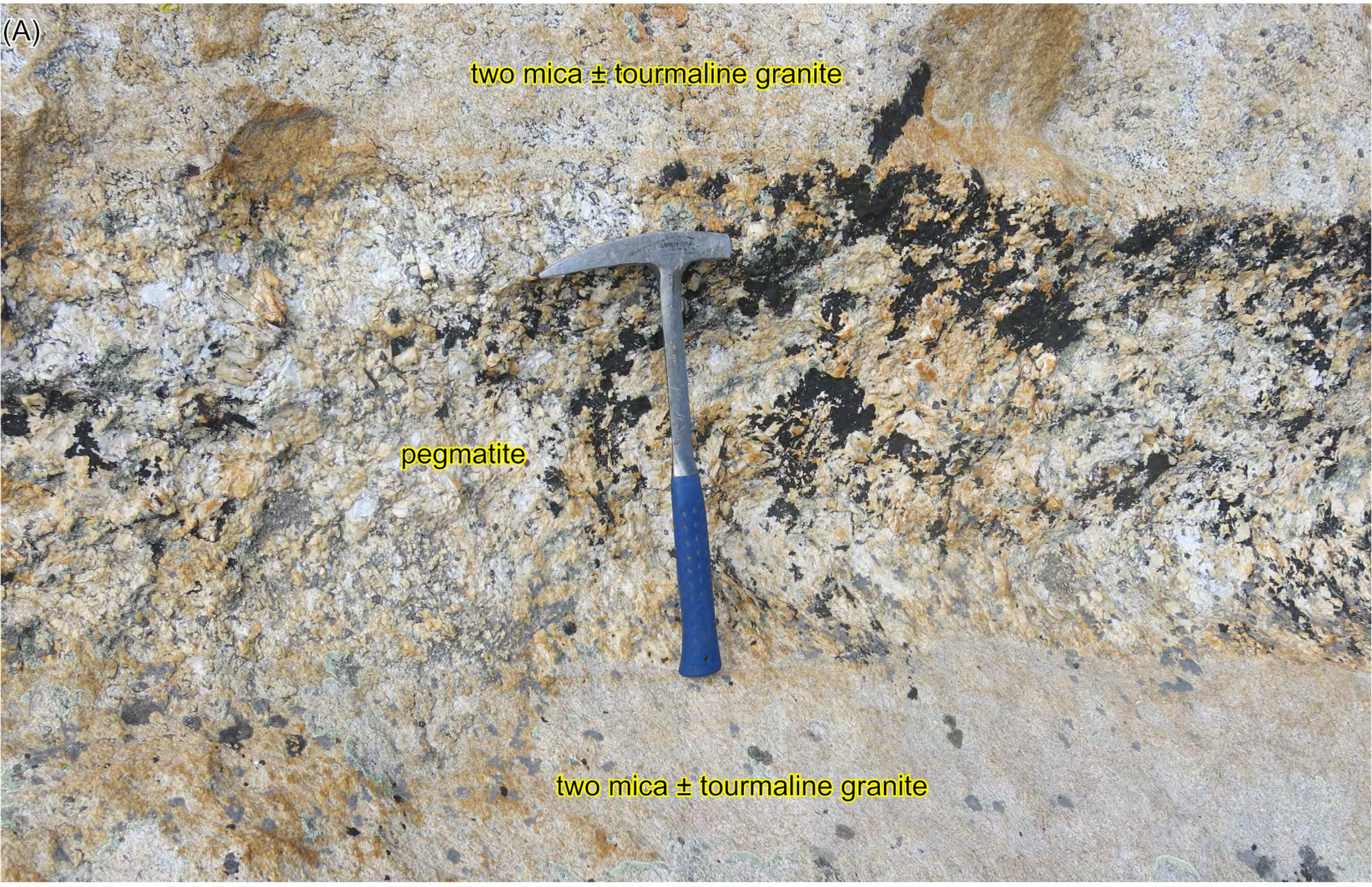
(A)
two mica ± tourmaline granite
pegmatite
two mica ± tourmaline granite
(B)
Figure 5A
Ms
Kfs
Qtz
Pl
Tur G
1 mm
(C)
Qtz
Tur P
5 mm

Figure 2

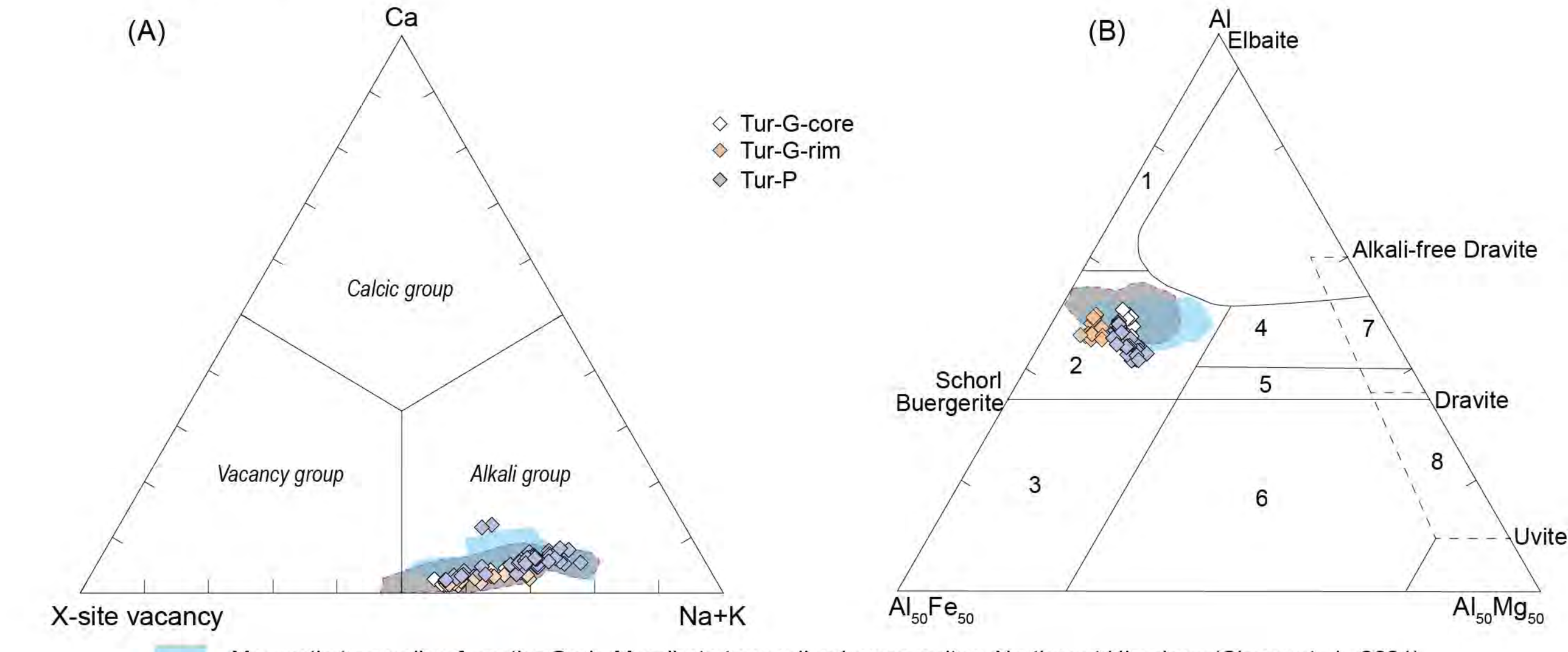
(A)
Ca
Calcic group
Vacancy group
Alkali group
X-site vacancy
Na+K
Tur-G-core
Tur-G-rim
Tur-P
(B)
Al
Elbaite
Alkali-free Dravite
Schorl
Buergerite
Dravite
Uvite
1
2
3
4
5
6
7
8
$Al_{50}Fe_{50}$
$Al_{50}Mg_{50}$
Magmatic tourmaline from the Gurla Mandhata tourmaline leucogranites, Northwest Himalaya (Cheng et al., 2021)
Magmatic tourmaline from the Nyalam leucogranites, South Tibetan Himalaya (Yang et al., 2015)

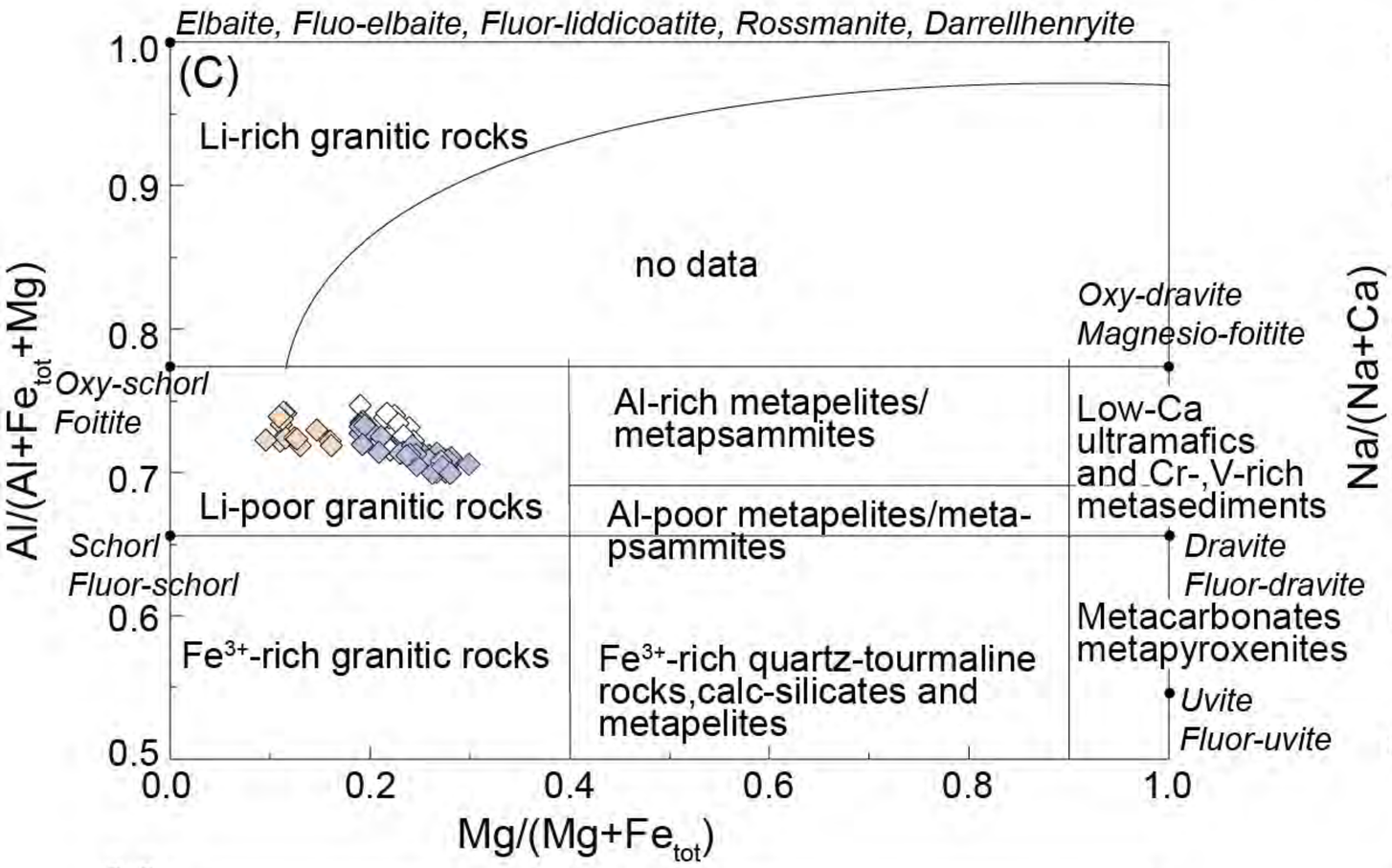
Elbaite, Fluo-elbaite, Fluor-liddicoatite, Rossmanite, Darrellhenryite
(C)
Li-rich granitic rocks
no data
Oxy-dravite
Magnesio-foitite
Oxy-schorl
Foitite
Al-rich metapelites/
metapsammites
Low-Ca
ultramafics
and Cr-,V-rich
metasediments
Li-poor granitic rocks
Al-poor metapelites/meta-
psammites
Schorl
Fluor-schorl
Dravite
Fluor-dravite
Fe3+-rich granitic rocks
Fe3+-rich quartz-tourmaline
rocks,calc-silicates and
metapelites
Metacarbonates
metapyroxenites
Uvite
Fluor-uvite
Al/(Al+Fetot+Mg)
Mg/(Mg+Fetot)
(D)
Schorl
Dravite
Na/(Na+Ca)
Mg/(Mg+Fe)

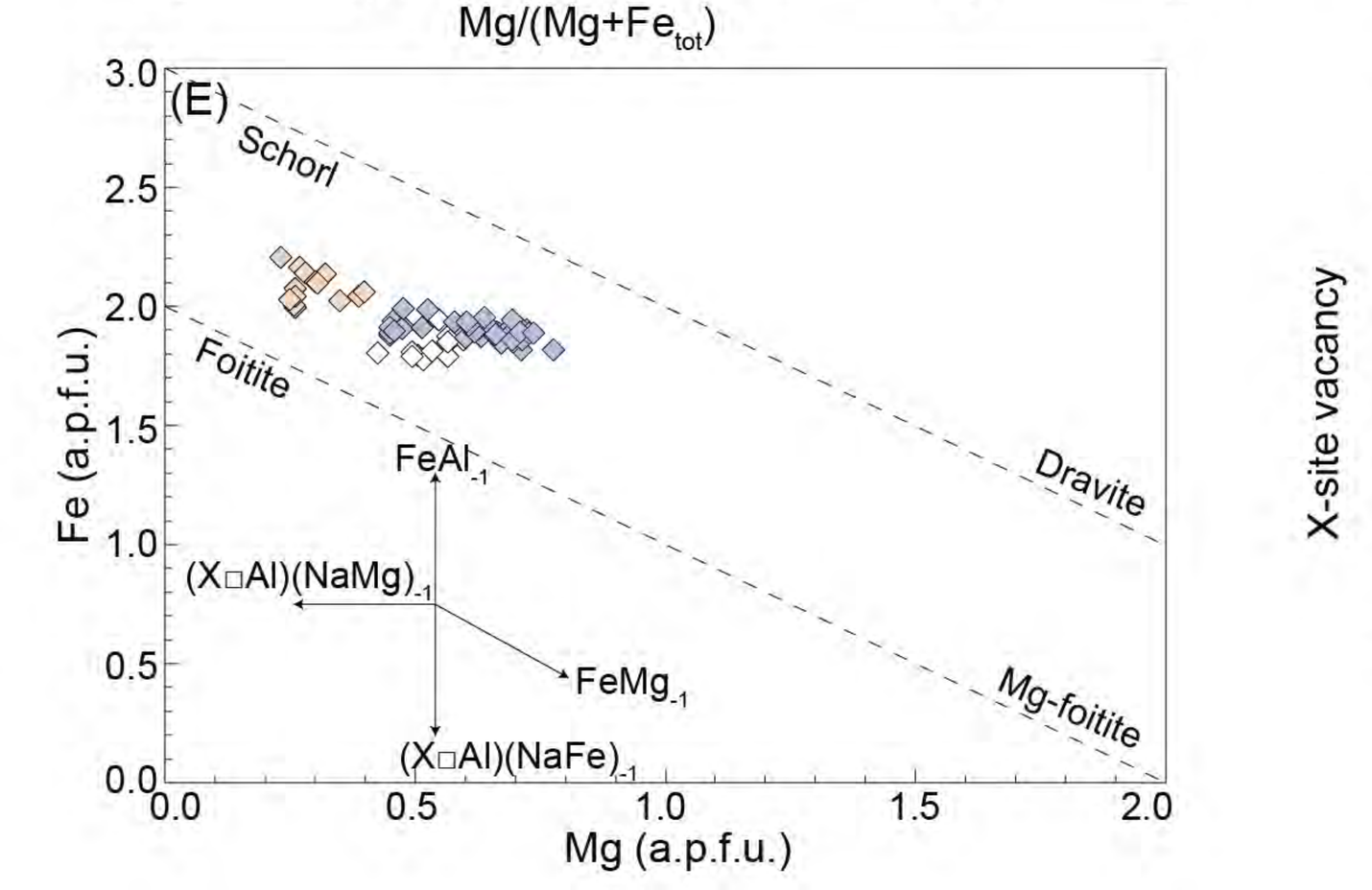
(E)
Schorl
Foitite
Dravite
Mg-foitite
FeAl-1
(X□Al)(NaMg)-1
FeMg-1
(X□Al)(NaFe)-1
Fe (a.p.f.u.)
Mg (a.p.f.u.)

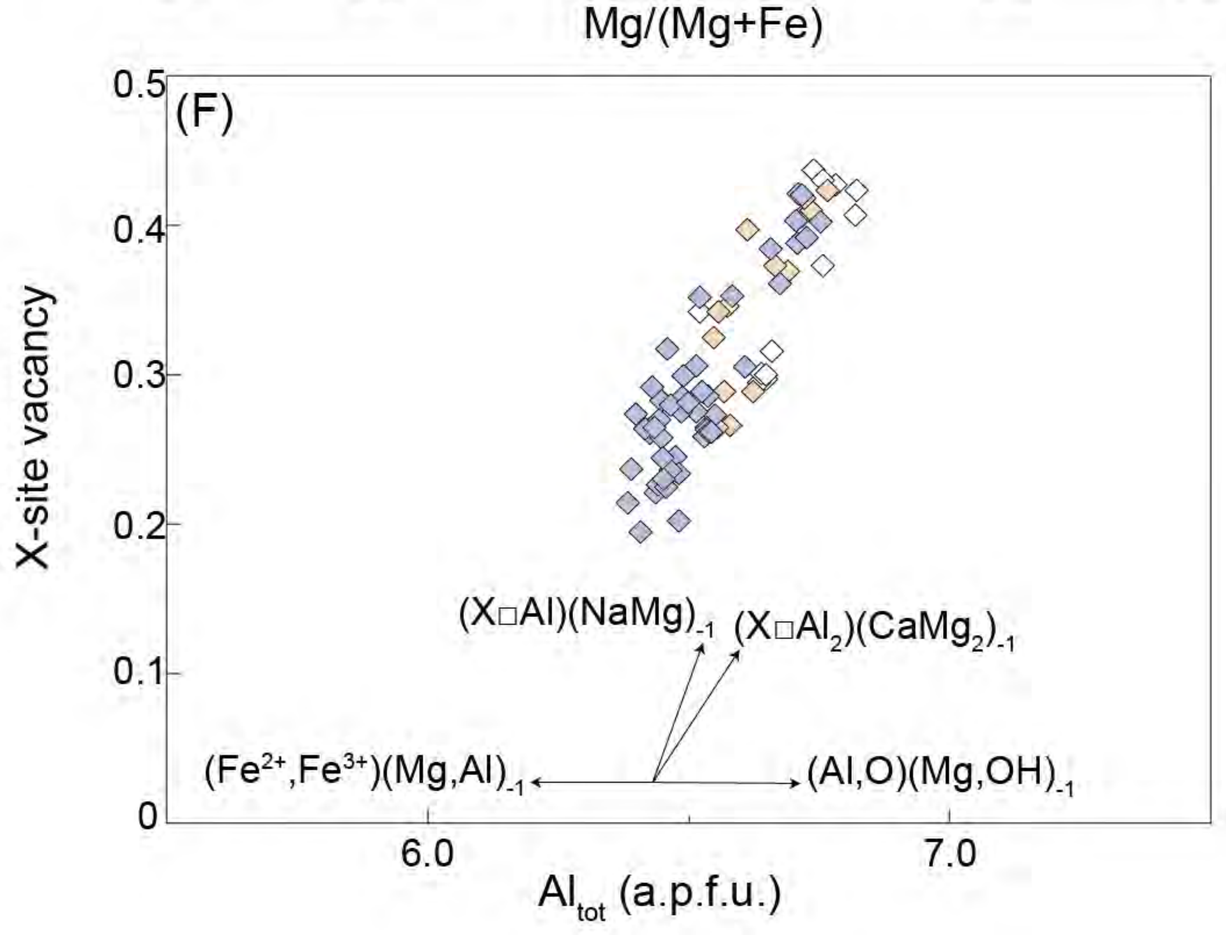
(F)
X-site vacancy
(X□Al)(NaMg)-1
(X□Al2)(CaMg2)-1
(Fe2+,Fe3+)(Mg,Al)-1
(Al,O)(Mg,OH)-1
Altot (a.p.f.u.)

Figure 3

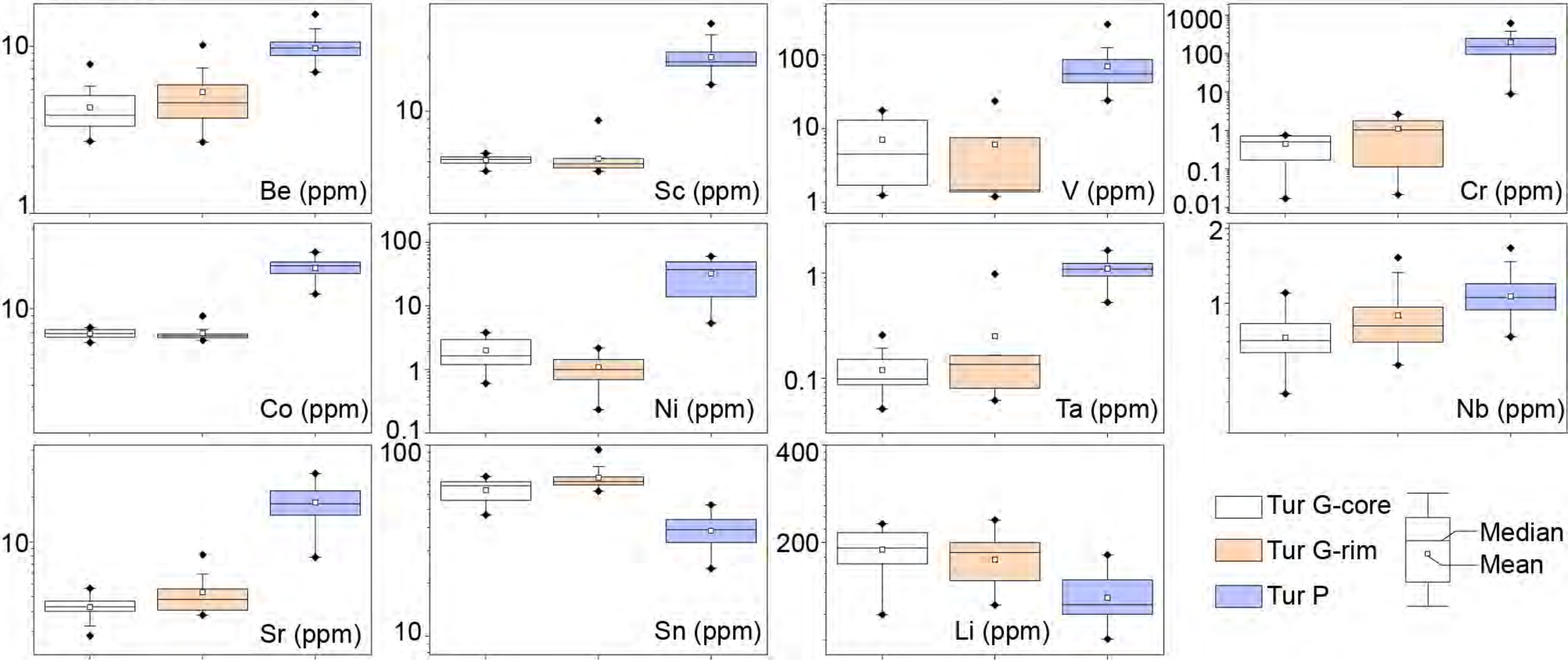
Be (ppm)
Sc (ppm)
V (ppm)
Cr (ppm)
Co (ppm)
Ni (ppm)
Ta (ppm)
Nb (ppm)
Sr (ppm)
Sn (ppm)
Li (ppm)
Tur G-core
Tur G-rim
Tur P
Median
Mean

Figure 4

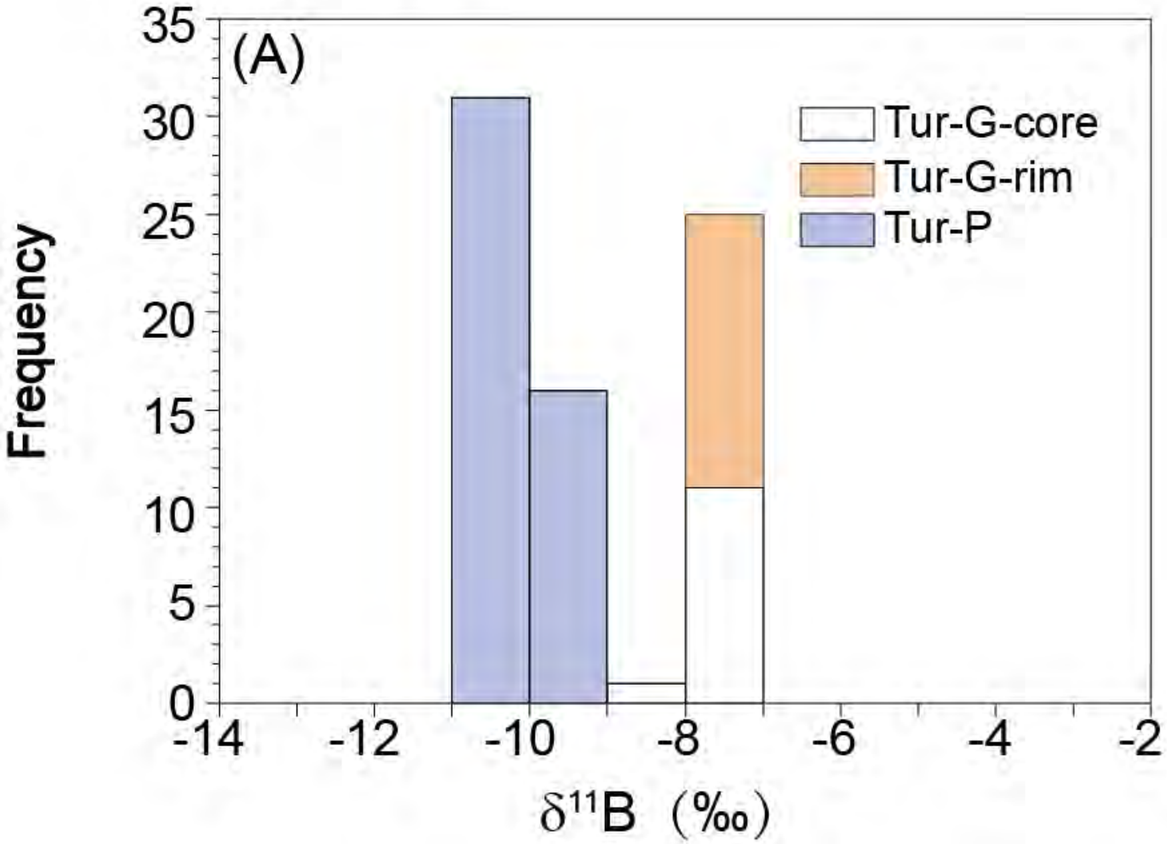
(A)
Tur-G-core
Tur-G-rim
Tur-P
Frequency
35
30
25
20
15
10
5
0
-14
-12
-10
-8
-6
-4
-2
δ11B (‰)

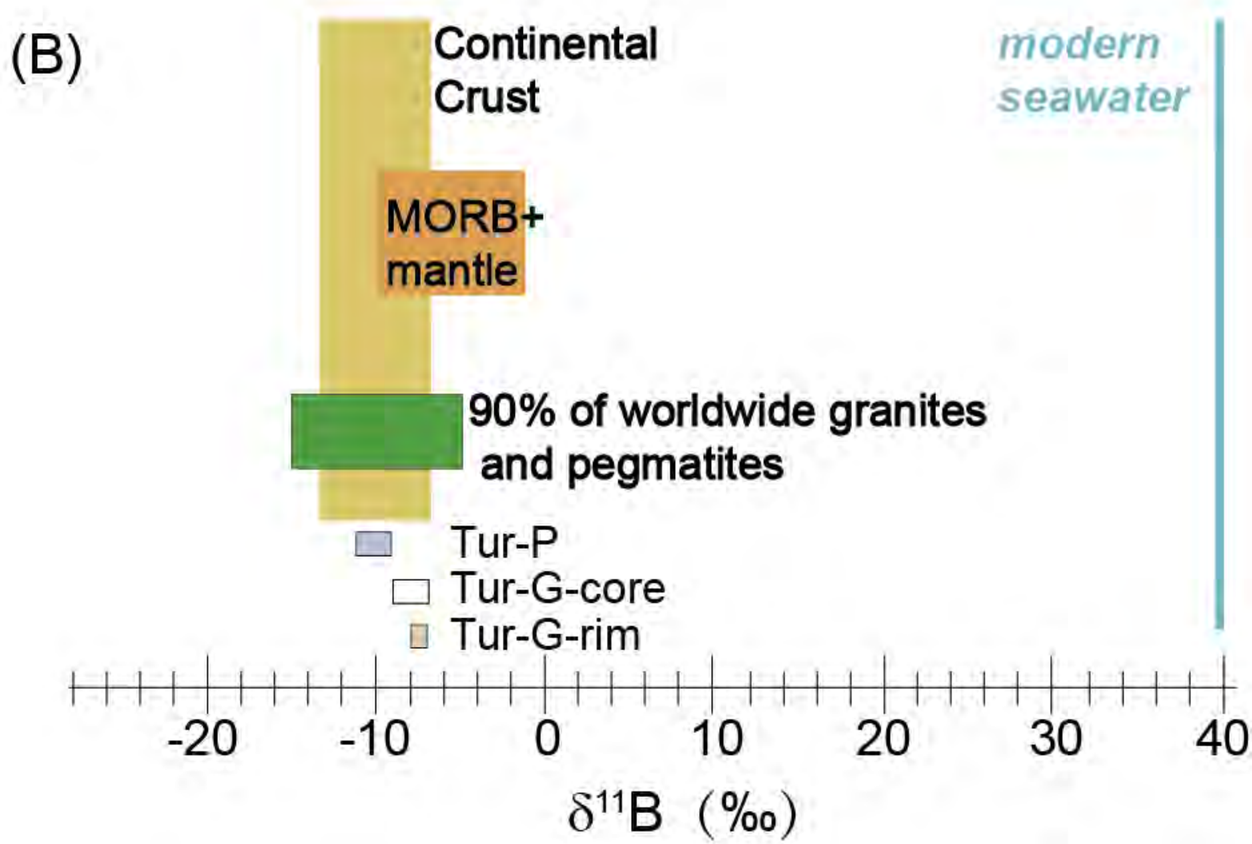
(B)
Continental Crust
modern seawater
MORB+ mantle
90% of worldwide granites and pegmatites
Tur-P
Tur-G-core
Tur-G-rim
-20
-10
0
10
20
30
40
δ11B (‰)

Figure 5

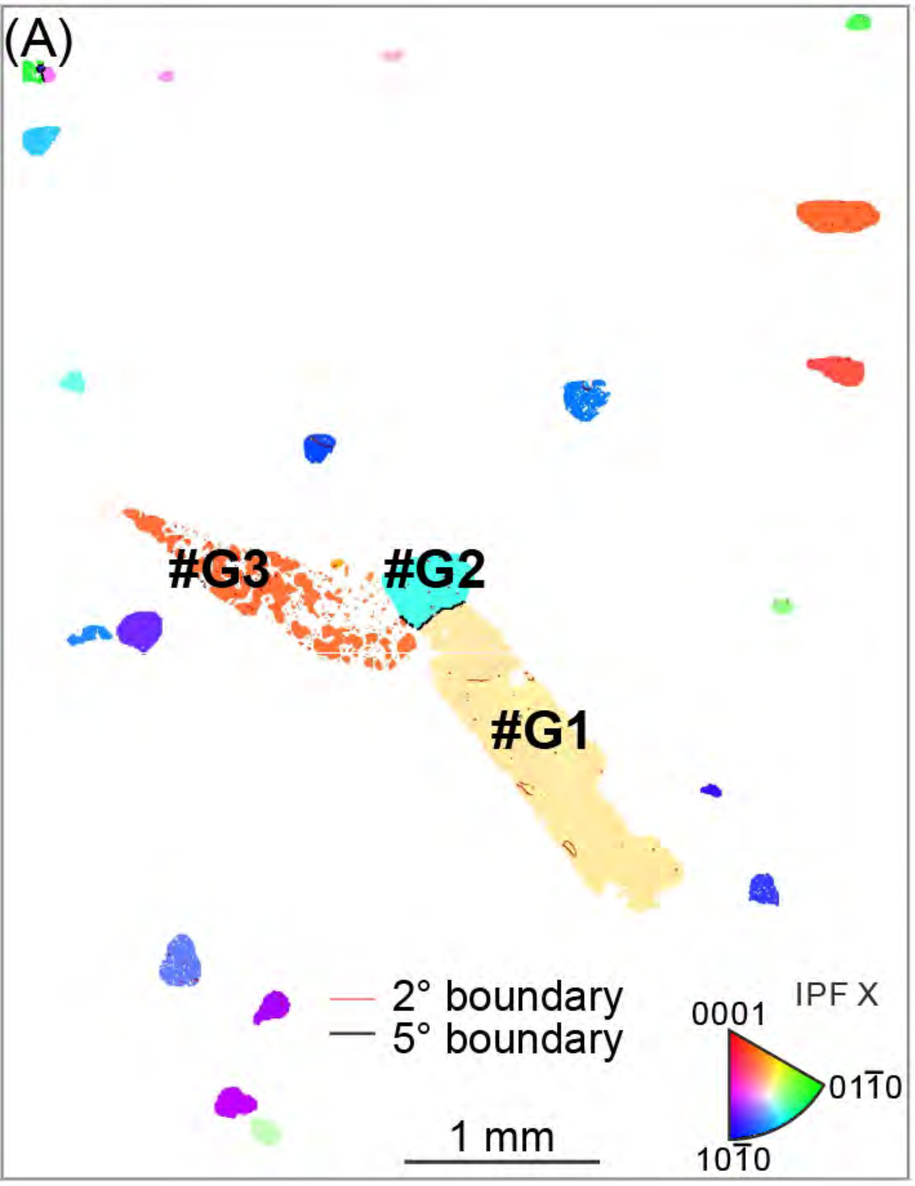
(A)
#G3
#G2
#G1
2° boundary
5° boundary
IPF X
0001
01$\bar{1}$0
10$\bar{1}$0
1 mm

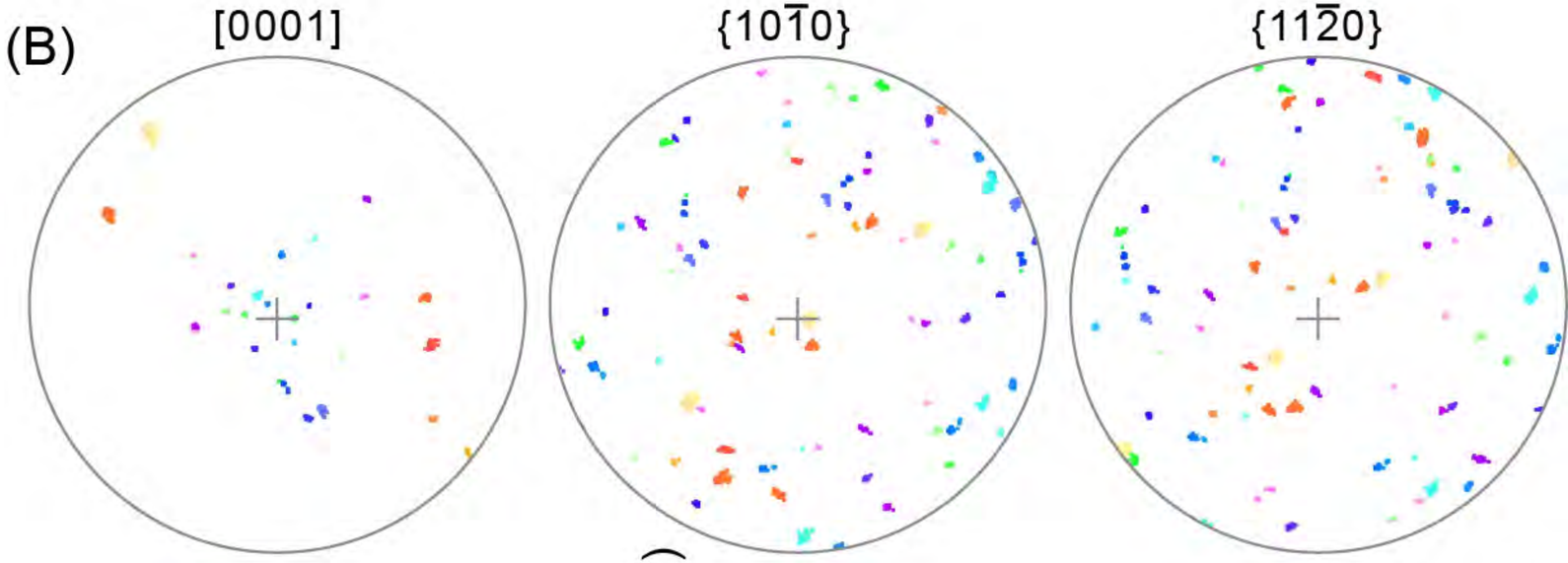
(B)
[0001]
{10$\bar{1}$0}
{11$\bar{2}$0}

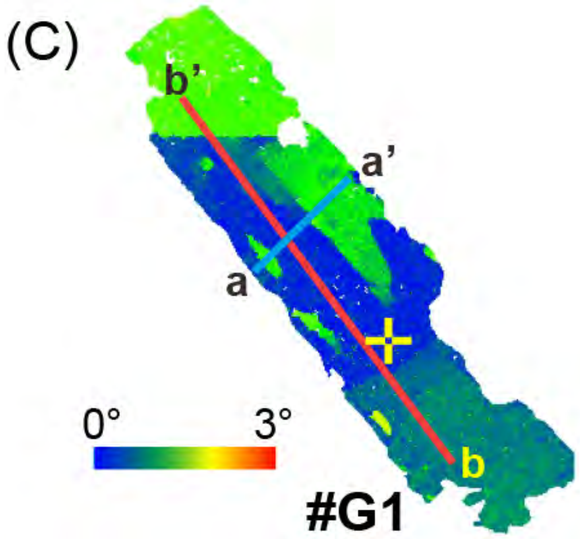
(C)
b'
a'
a
b
0°
3°
#G1

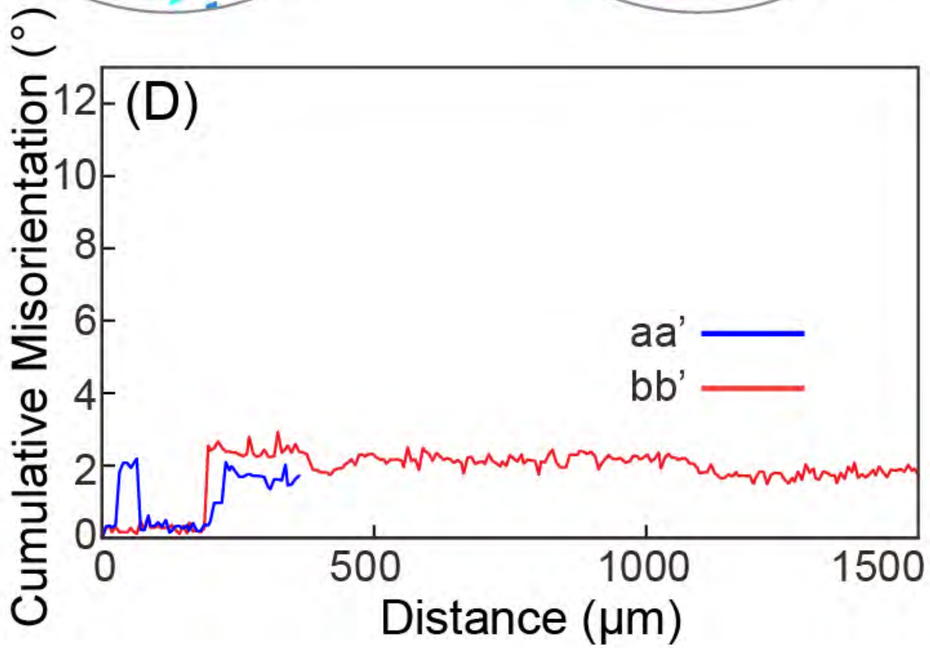
(D)
Cumulative Misorientation (°)
0
2
4
6
8
10
12
0
500
1000
1500
Distance (μm)
aa'
bb'

Figure 6

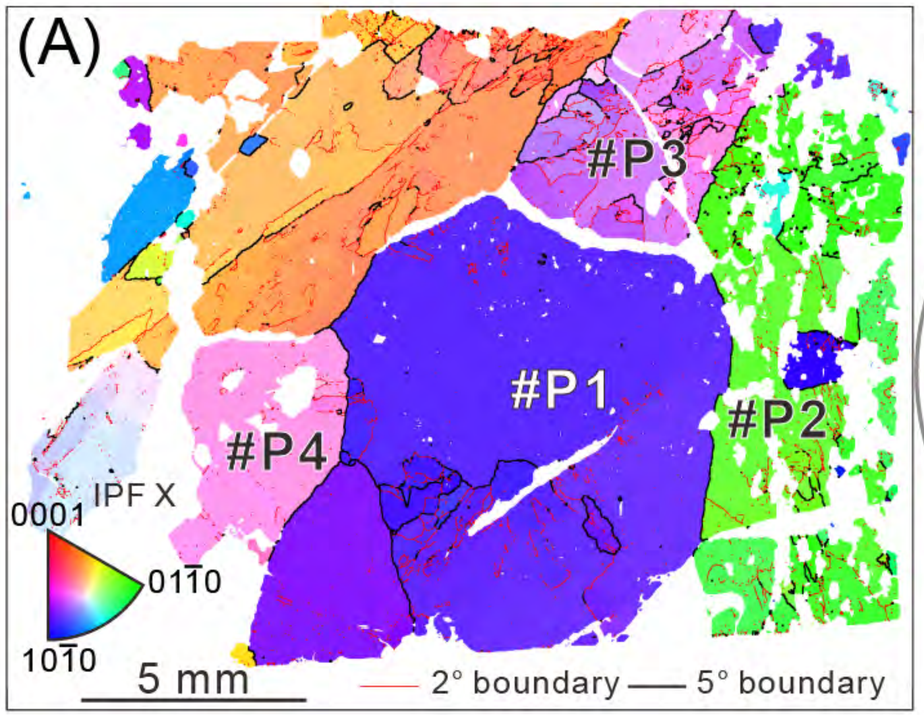
(A)
#P3
#P1
#P2
#P4
IPF X
0001
01$\bar{1}$0
10$\bar{1}$0
5 mm
2° boundary
5° boundary

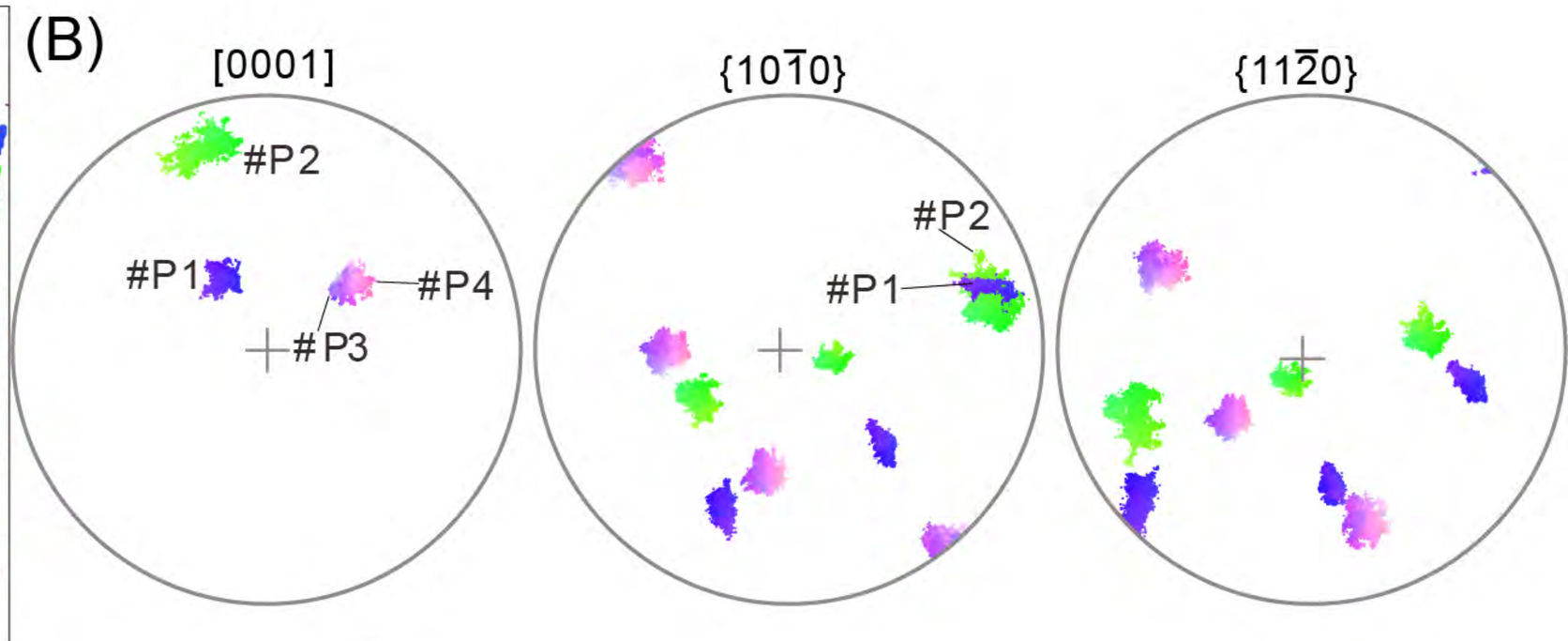
(B)
[0001]
{10$\bar{1}$0}
{11$\bar{2}$0}
#P2
#P1
#P4
#P3
#P2
#P1

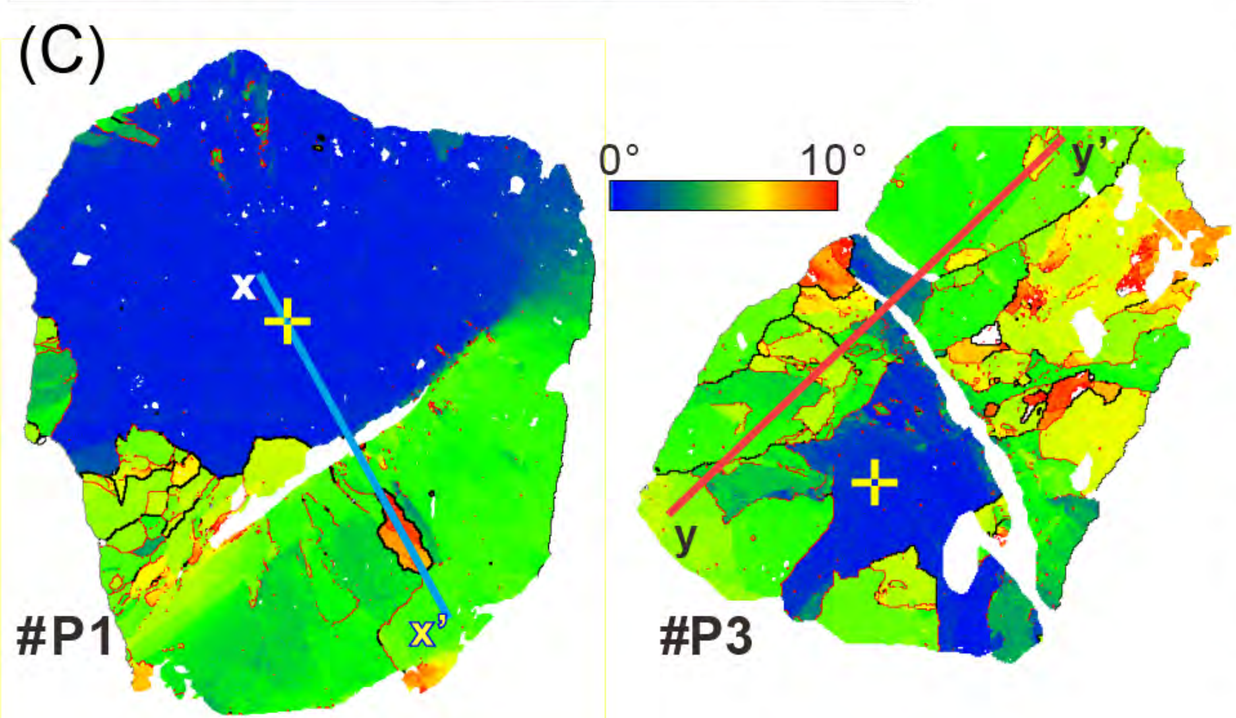
(C)
0°
10°
x
x'
y
y'
#P1
#P3

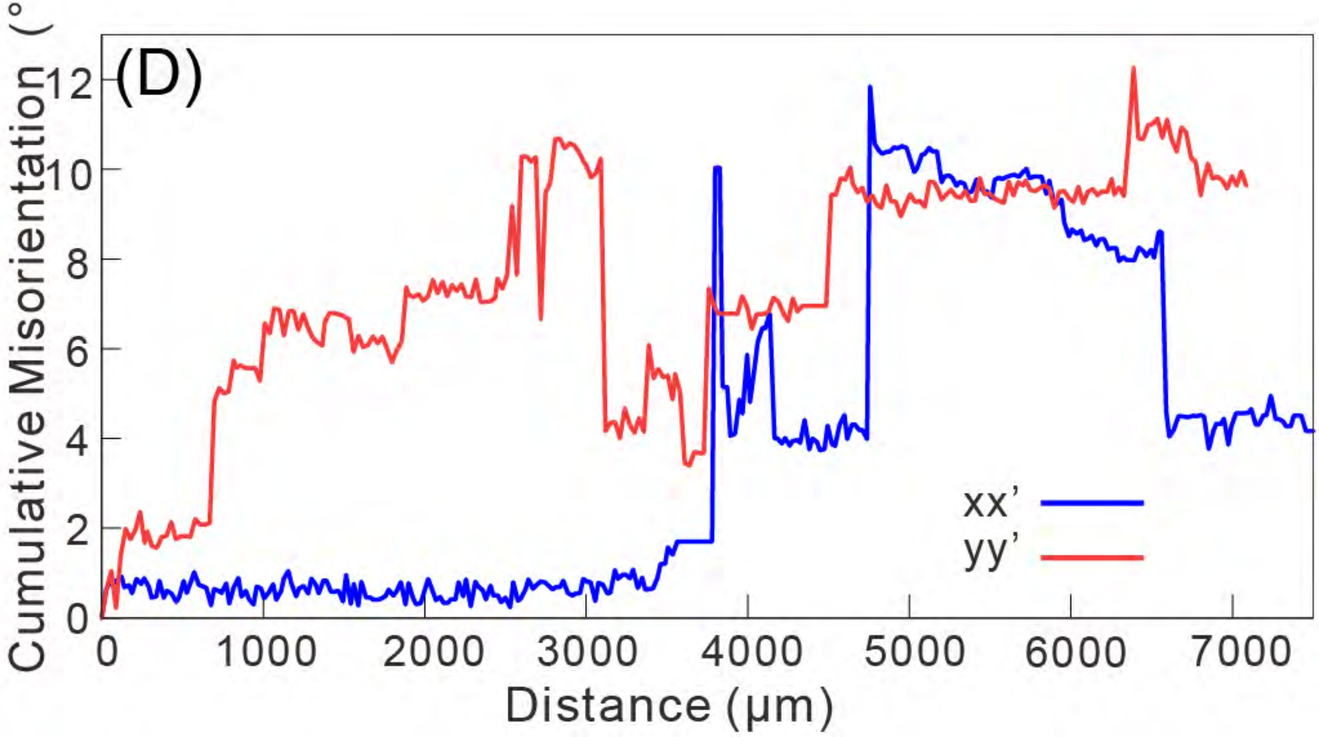
(D)
Cumulative Misorientation (°)
0
2
4
6
8
10
12
0
1000
2000
3000
4000
5000
6000
7000
Distance (μm)
xx'
yy'

Figure 7

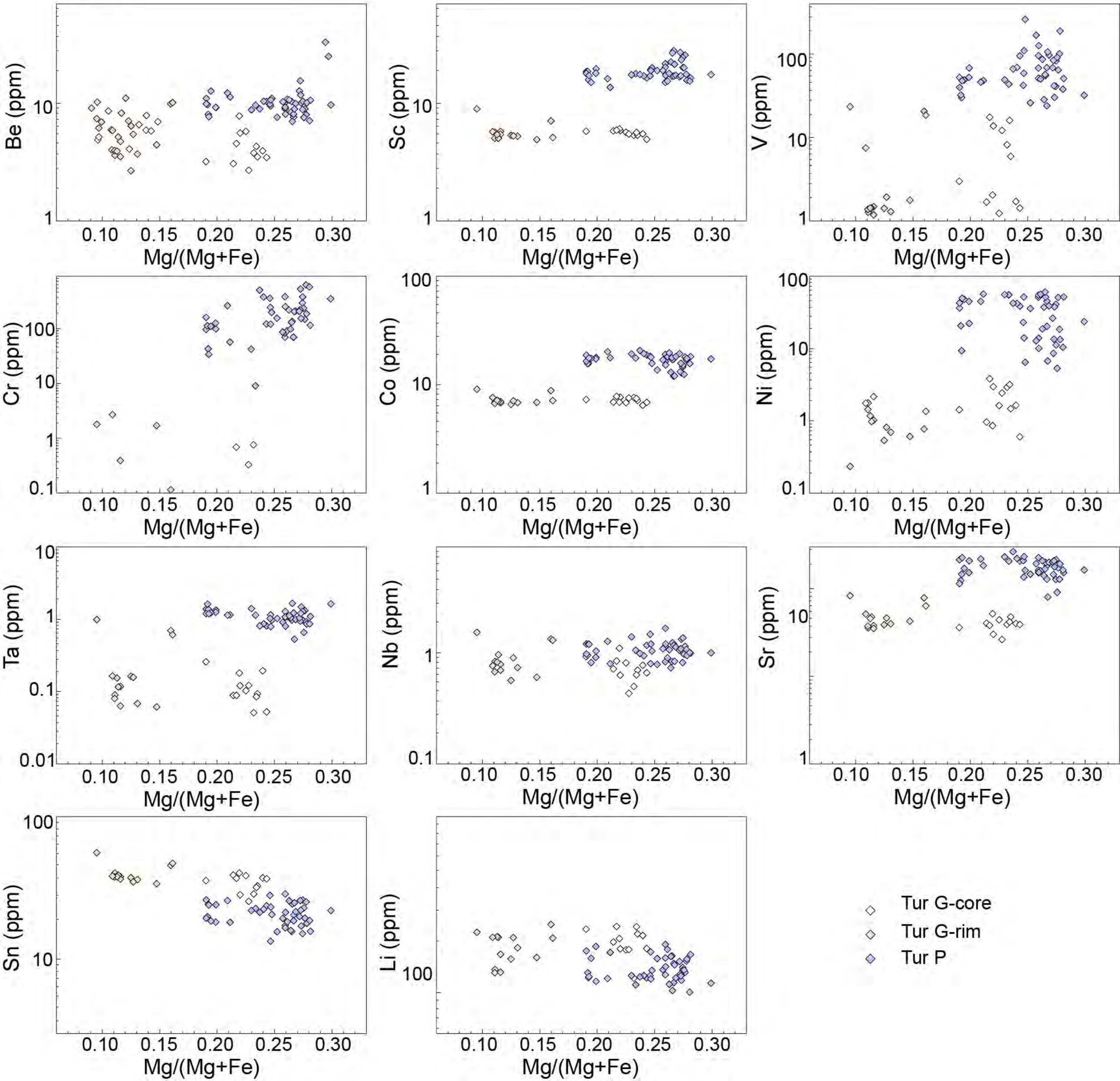
Be (ppm)
Sc (ppm)
V (ppm)
Cr (ppm)
Co (ppm)
Ni (ppm)
Ta (ppm)
Nb (ppm)
Sr (ppm)
Sn (ppm)
Li (ppm)
Mg/(Mg+Fe)
Tur G-core
Tur G-rim
Tur P

Figure 8

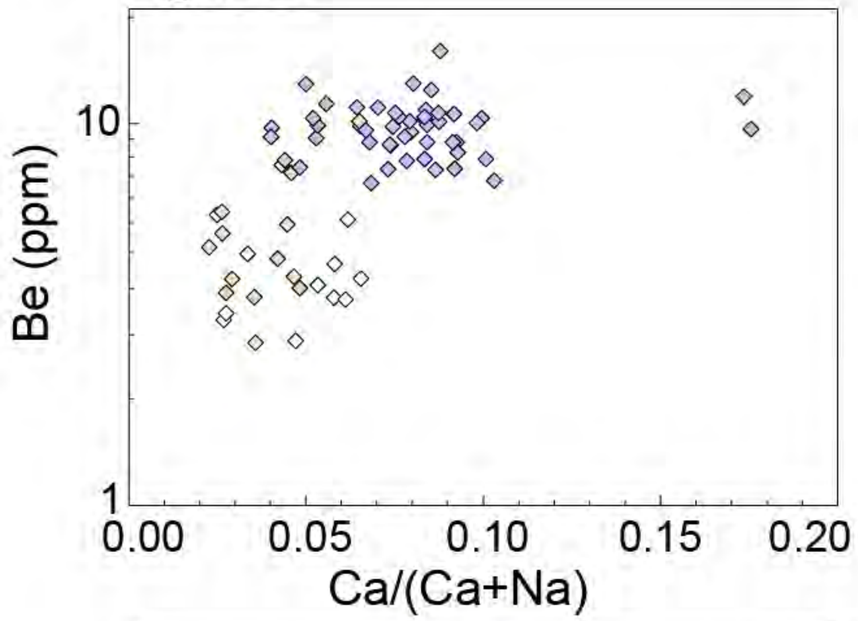
Be (ppm)
10
1
0.00
0.05
0.10
0.15
0.20
Ca/(Ca+Na)

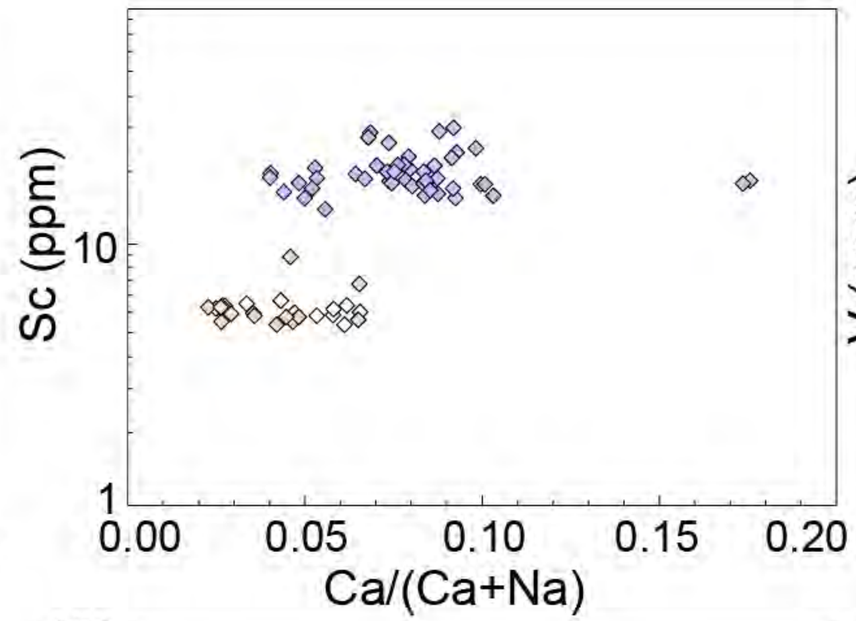
Sc (ppm)
10
1
0.00
0.05
0.10
0.15
0.20
Ca/(Ca+Na)

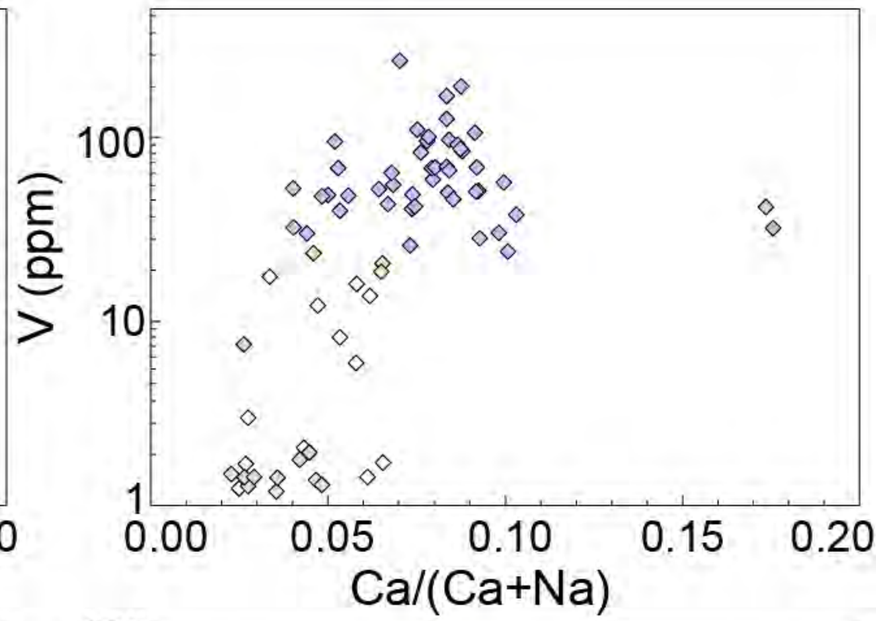
V (ppm)
100
10
1
0.00
0.05
0.10
0.15
0.20
Ca/(Ca+Na)

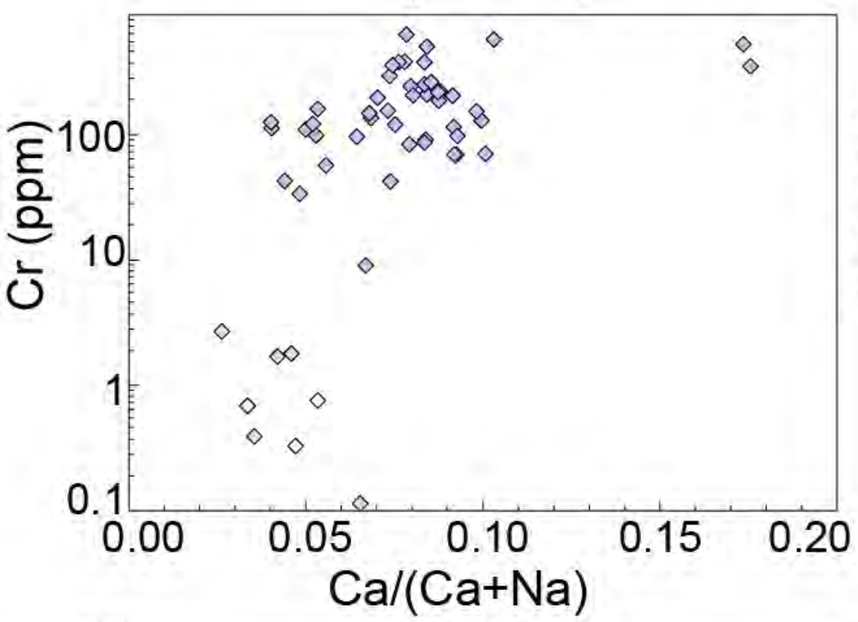
Cr (ppm)
100
10
1
0.1
0.00
0.05
0.10
0.15
0.20
Ca/(Ca+Na)

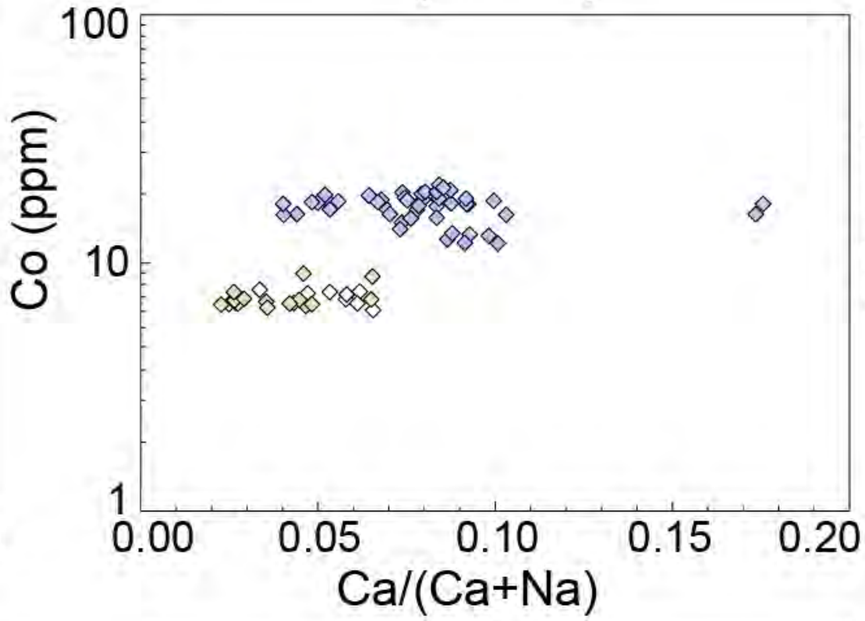
Co (ppm)
100
10
1
0.00
0.05
0.10
0.15
0.20
Ca/(Ca+Na)

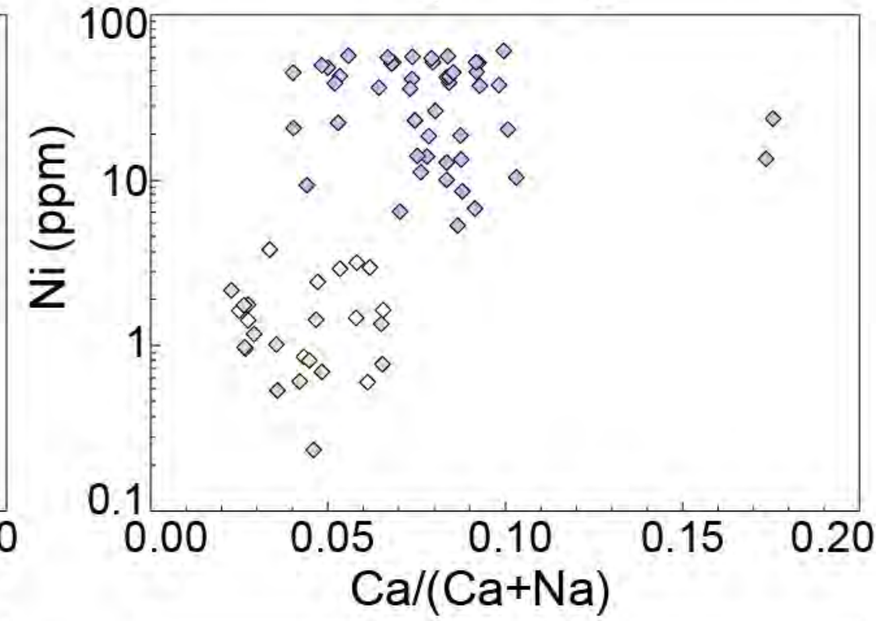
Ni (ppm)
100
10
1
0.1
0.00
0.05
0.10
0.15
0.20
Ca/(Ca+Na)

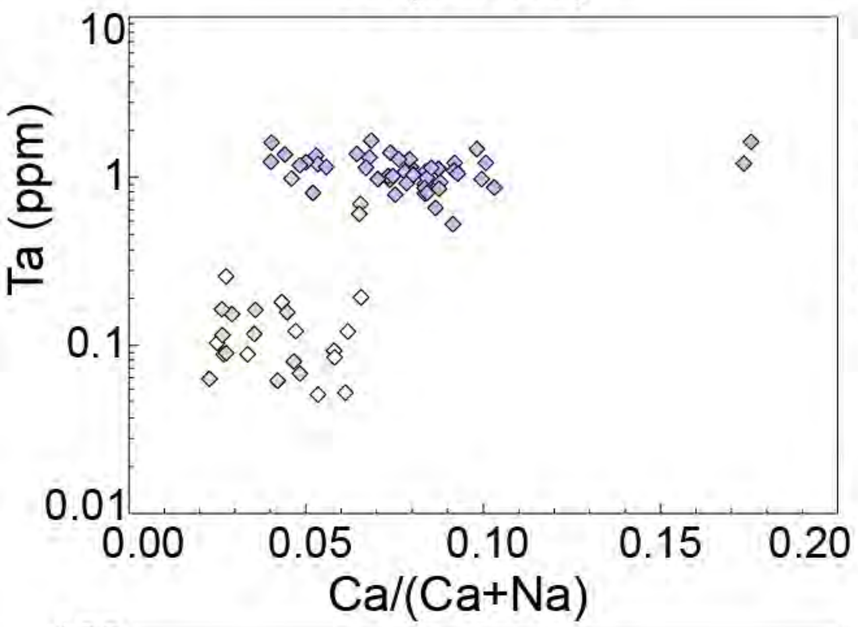
Ta (ppm)
10
1
0.1
0.01
0.00
0.05
0.10
0.15
0.20
Ca/(Ca+Na)

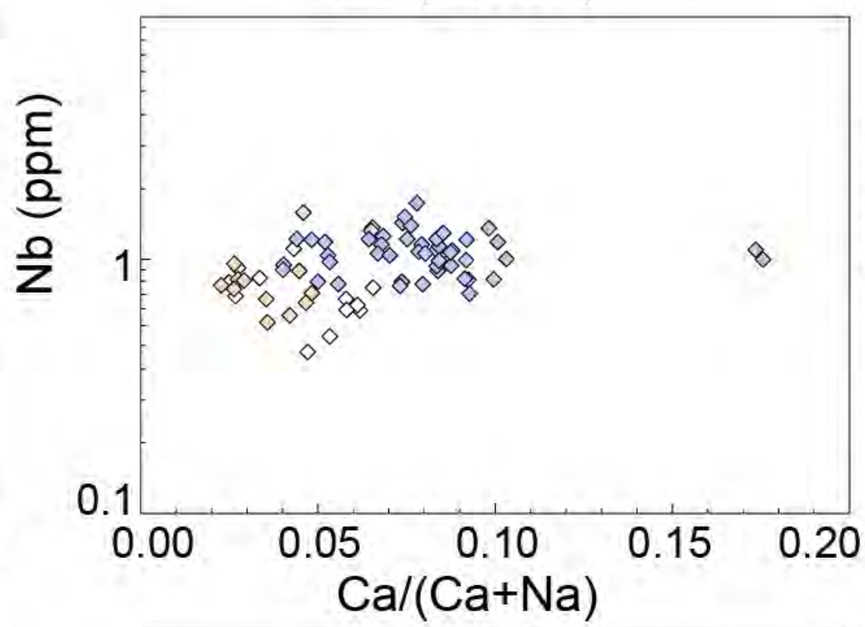
Nb (ppm)
1
0.1
0.00
0.05
0.10
0.15
0.20
Ca/(Ca+Na)

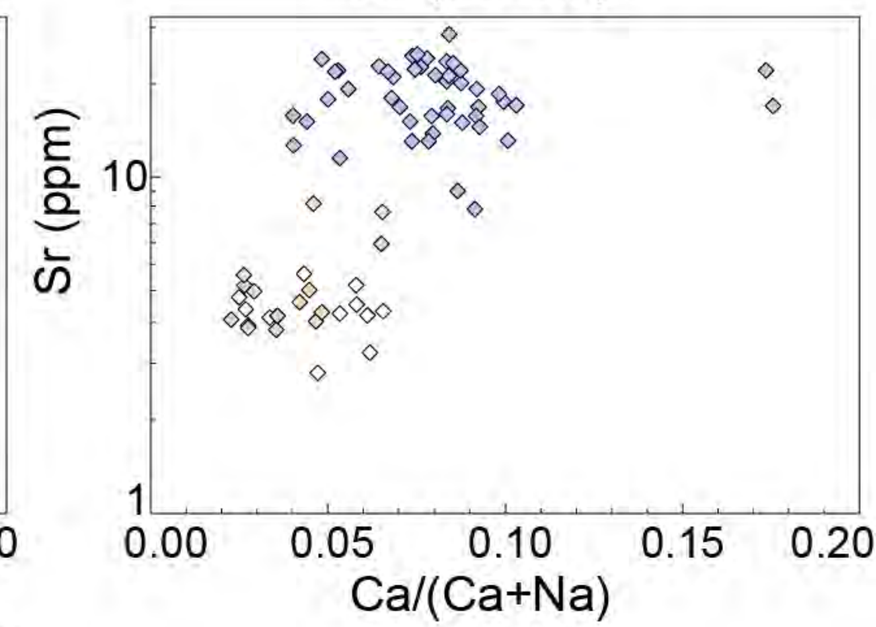
Sr (ppm)
10
1
0.00
0.05
0.10
0.15
0.20
Ca/(Ca+Na)

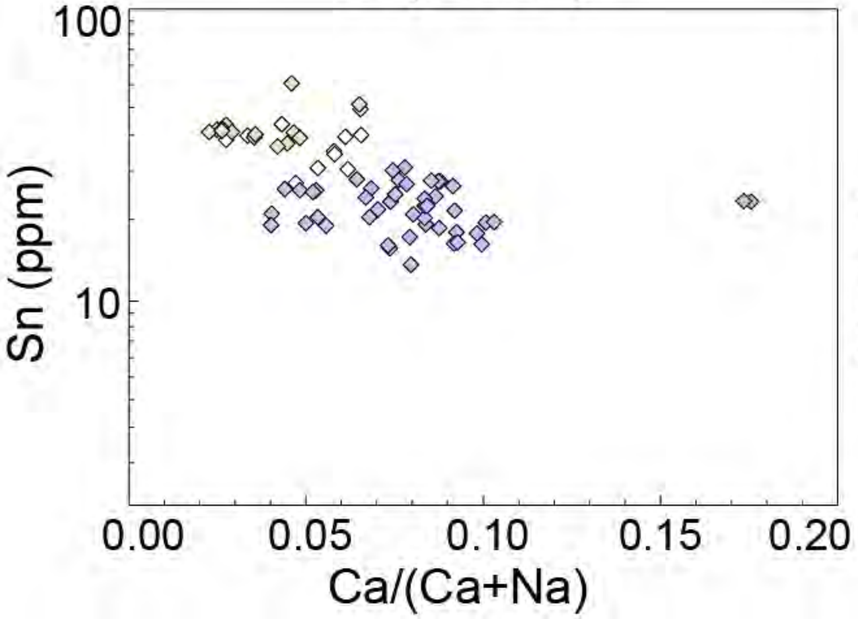
Sn (ppm)
100
10
0.00
0.05
0.10
0.15
0.20
Ca/(Ca+Na)

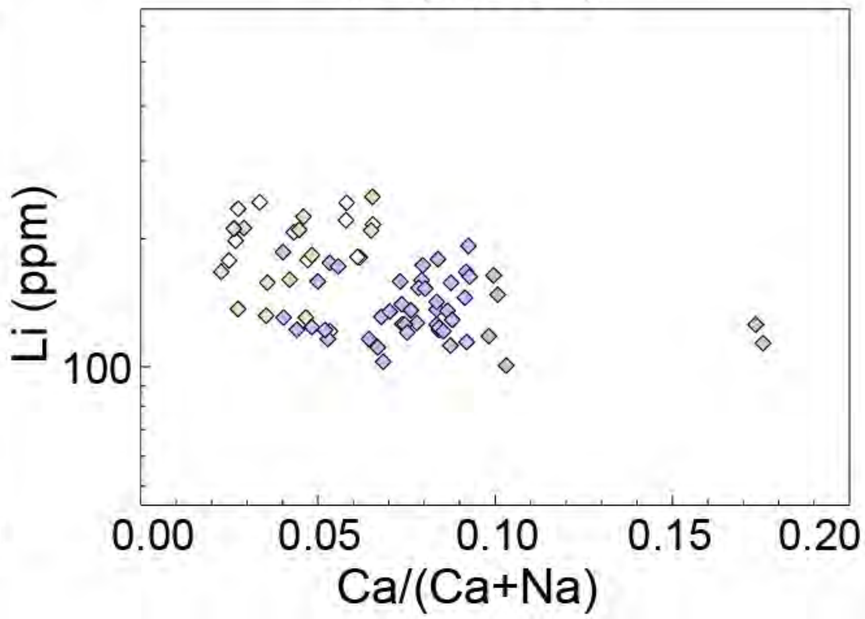
Li (ppm)
100
0.00
0.05
0.10
0.15
0.20
Ca/(Ca+Na)

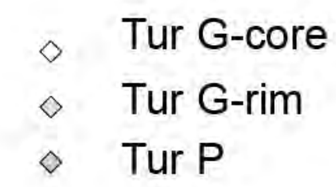
Tur G-core
Tur G-rim
Tur P